1995SoPh..162..189W

SUMER – SOLAR ULTRAVIOLET MEASUREMENTS OF EMITTED RADIATION

K. WILHELM, W. CURDT, E. MARSCH and U. SCHÜHLE
Max-Planck-Institut für Aeronomie
D-37189 Katlenburg-Lindau, Germany
P. LEMAIRE, A. GABRIEL and J.-C. VIAL
Institut d'Astrophysique Spatiale, Unite Mixte CNRS – Université
Paris XI, Bat 121, F-91405 Orsay, France
M. GREWING
Astronomisches Institut, D-72076 Tübingen, Germany
M.C.E. HUBER
ESA, Space Science Department, ESTEC,
NL-2200 AG Noordwijk, The Netherlands
S.D. JORDAN, A.I. POLAND and R.J. THOMAS
NASA/Goddard Space Flight Center
Greenbelt, Maryland, USA
M. KÜHNE
Physikalisch-Technische Bundesanstalt, D-10587 Berlin, Germany
J.G. TIMOTHY
The University of New Brunswick, Fredericton, Canada
D.M. HASSLER
High Altitude Observatory/NCAR, Boulder, Colorado, USA
and
O.H.W. SIEGMUND
The University of California, SSL, Berkeley, California, USA

Abstract. The instrument SUMER – Solar Ultraviolet Measurements of Emitted Radiation is designed to investigate structures and associated dynamical processes occurring in the solar atmosphere, from the chromosphere through the transition region to the inner corona, over a temperature range from 10^4 to 2×10^6 K and above. These observations will permit detailed spectroscopic diagnostics of plasma densities and temperatures in many solar features, and will support penetrating studies of underlying physical processes, including plasma flows, turbulence and wave motions, diffusion transport processes, events associated with solar magnetic activity, atmospheric heating, and solar wind acceleration in the inner corona. Specifically, SUMER will measure profiles and intensities of EUV lines; determine Doppler shifts and line broadenings with high accuracy; provide stigmatic images of the Sun in the EUV with high spatial, spectral, and temporal resolution; and obtain monochromatic maps of the full Sun and the inner corona or selected areas thereof. SUMER will be flown on the Solar and Heliospheric Observatory (SOHO), scheduled for launch in November, 1995. This paper has been written to familiarize solar physicists with SUMER and to demonstrate some command procedures for achieving certain scientific observations.

Key words: Solar EUV Emission Lines – Coronal Heating – Solar Wind Acceleration – EUV Spectrometer

Solar Physics **162**: 189–231, 1995.

1. Overview

The SUMER telescope and spectrometer has been built to make high-resolution solar observations over the broad wavelength range from less than 500 to 1610 Å. Spectral imaging of the Sun with short exposure times in the EUV emission lines in this range will allow us to study essential physical parameters of the solar atmosphere: plasma density and temperature, abundances of species, velocity fields, topologies of the plasma structures and their evolution at high temporal resolution of a few seconds. The instrument has also been designed to be as user friendly as possible, with both Predefined Operational Programmes (POP, cf. Section 4.6.) that can be implemented by an execution command and User Defined Programmes (UDP, cf. Section 4.7.) that are easy to generate with the command structure provided. A description of the instrument and the associated command procedures is provided below, to assist the user scientist in the construction and execution of observing programmes.

SUMER observations in carefully selected chromospheric, transition region and coronal lines will be made on the solar disk and off the limb in the inner corona, and will permit density and temperature diagnostics of solar features approaching 1 *arcsec* in angular resolution, or approximately 1000 *km* in spatial extent. This high spatial resolution will permit fine-scale observations and thus greatly improve and foster detailed modelling of solar structures.

High resolution measurements are of prime importance for the following areas of science:

- Solar physics. *Coronal heating:* The existence of a corona requires a persistent energy input to compensate for radiative and conductive losses and for the solar wind expansion. The presence of any non-radiative mechanical heating mechanism should manifest itself by velocity fluctuations, which may be detected by optical means in terms of line broadenings and Doppler shifts. *Solar wind acceleration:* Modern concepts of high-speed solar wind acceleration hinge on the amount of wave energy available in the corona to drive the wind by wave pressure gradient forces, although it is also possible that the solar wind represents the accumulated effect of many small isolated acceleration sites. *Structure of the solar upper atmosphere:* At the base of the corona small and large inhomogeneities are in a continuous state of fluctuation on time scales ranging from seconds to days and sometimes weeks.
- Stellar physics. Many stars have coronae and winds. The Sun is the only star where theoretical concepts of coronal heating and wind generation mechanisms may be tested observationally by resolving the plasma processes.
- Plasma physics. The topology of the solar plasma structures is defined by magnetic fields, which are rooted in the photosphere and convection zone. This natural plasma environment accessible to detailed observations offers a

1995SoPh..162..189W

valuable opportunity to improve, by transfer of knowledge, our understanding of astrophysical and laboratory plasmas.

- Solar-terrestrial relationship. The Earth, in common with the other planets, is immersed in the solar wind and radiation field. The terrestrial atmosphere responds dynamically and chemically to photons and particles expelled from the Sun. A systematic study of the solar plasma and the solar wind is required to establish a better understanding of magnetospheric as well as middle- and upper-atmospheric phenomena.

The SUMER capabilities are complementary to those of the other instruments on SOHO, especially the Coronal Diagnostic Spectrometer (CDS) (Harrison et al., 1995). They include: (i) A spatial resolution compatible with the spacecraft constraints. (ii) An effective, relative spectral resolving power in the full wavelength range of approximately 3×10^5, in order to determine line-of-sight velocities from Doppler shifts with an accuracy of about 1 $km\ s^{-1}$ and to estimate wave amplitudes. (iii) A temporal resolution down to 1 s or less in some strong lines, to follow dynamically evolving features like jets and bright points, and to resolve wave motions at the lower limit of periods expected.

The study of many solar phenomena does not need such high temporal resolution, but does need continuous time coverage. Examples are the chromospheric network and its extension into the corona, and active-region loops. Measurements of the lifetimes and periodicities, and the growth and decay rates of such structures at different wavelengths will provide a better picture of solar variability. Ideally, observations of these phenomena should proceed over extended periods of time with no interruptions. For this reason, the SOHO spacecraft, in its halo orbit around the L1 libration point, is an excellent platform from which to make such observations.

We expect to study solar structures down to the 1-*arcsec* level and events down to the 1-s time scale in the SUMER wavelength range. This spectral coverage will be further extended to shorter wavelengths in the CDS instrument. Some of the lines observable over the full range covered by the two instruments are shown in Figure 1. Also indicated are the wavelength ranges and lines covered by the UVCS and EIT instruments (Kohl et al., 1995; Delaboudinière et al., 1995).

Existing EUV observations are clearly inadequate to determine physical properties of coronal structures with enough precision to discriminate between different models. Previously flown EUV imaging instruments have generally obtained angular resolutions of > 5 *arcsec*, with many images obtained in the 15–60-*arcsec* range. Such resolution may be adequate to study the gross properties of relatively large features like active regions and coronal holes, but it is clearly inadequate for studies of the detailed structure and dynamics of the corona, and of other properties that typically reveal the underlying physics.

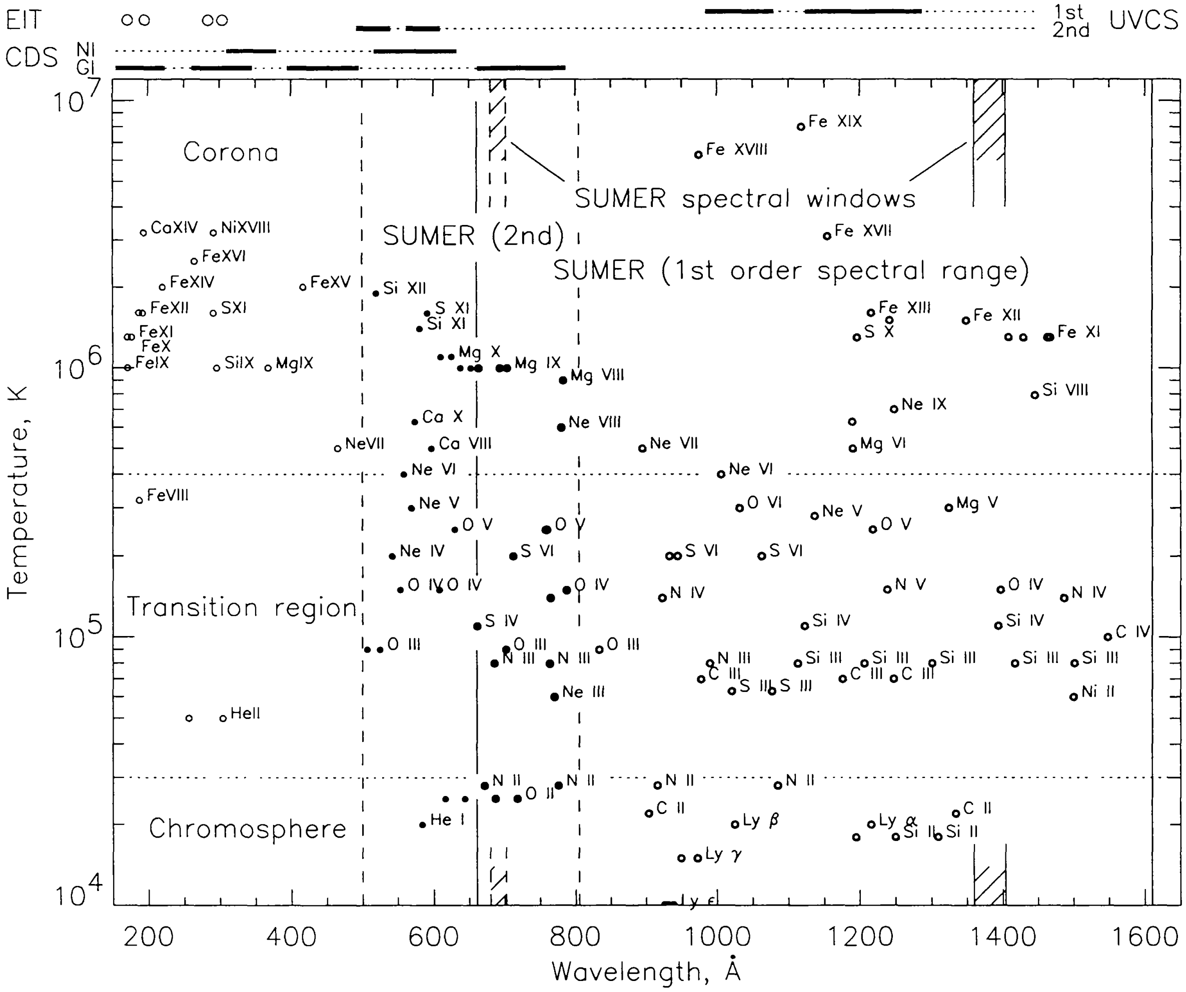

Fig. 1. Selection of emission lines in the wavelength range from 150 to 1610 Å together with the corresponding SUMER, CDS, UVCS and EIT coverages. Observations from 500 to 805 Å can be performed by SUMER in 2nd order and from 661 to 1610 Å in 1st order. The instantaneous coverage is approximately 22 Å in 2nd order and 44 Å in 1st order. This is indicated for a specific wavelength setting (for details see Section 2.1.). The short-wavelength region will be observed by CDS in its NI (normal incidence) and GI (grazing incidence) bands as indicated in the upper margin. Note the overlap in wavelength bands of all instruments, which will be important for inter-calibration.

Measurements of the intensity ratio of certain selected EUV line pairs can give direct knowledge of electron density N_e or electron temperature T_e in the emitting source, since the excitation mechanism for many such lines depends critically on these two plasma parameters (cf. Dwivedi, 1994). For example, coronal lines are generally formed by collisional excitation from and radiative decay to the ground level, where the bulk of the ion population resides. However, if the radiative decay rate is small (i.e., for forbidden or intersystem transitions), collisional de-excitation processes become more important as the electron density increases and the populations of the upper (metastable) levels become comparable to that of the ground lev-

TABLE I

Some line pairs useful for electron density or temperature diagnostic studies with SUMER. (Expected counting rates are given for active regions.)

Ion	Wavelength, Å	Electron density, N_e, *electron* cm^{-3}	Temperature, T_e, *K*	Intensity, (*count* s^{-1} *arcsec*$^{-2}$)
S X	1213/1196	$2.0 \times 10^8 - 2.0 \times 10^{10}$	1.2×10^6	20/8
C III	1175/977	$1.0 \times 10^9 - 1.0 \times 10^{10}$	7.0×10^4	1024/1340
	1247/1175	$1.0 \times 10^9 - 1.0 \times 10^{10}$	7.0×10^4	2/1024
O V	760/629	$1.0 \times 10^9 - 1.0 \times 10^{10}$	2.5×10^5	6/59
N IV	923/765	$1.0 \times 10^9 - 1.0 \times 10^{11}$	1.4×10^5	24/4
Si III	1312/1301	$1.0 \times 10^9 - 1.0 \times 10^{11}$	3.5×10^4	11/33
O IV	1407/1404	$3.0 \times 10^9 - 3.0 \times 10^{11}$	1.7×10^5	5/6
O IV	790/553		$8.0 \times 10^4 - 2.0 \times 10^5$	15/10
N III	991/686		$< 7.0 \times 10^4$	138/3
O VI	1032/173*		$3.0 \times 10^5 - 1.0 \times 10^6$	1102/*

* *Coronal Diagnostic Spectrometer (CDS) observation*

el. The intensity of spectral lines involving these transitions will then be directly related to the electron density of the source region (Gabriel & Jordan, 1969). By taking the intensity ratio against a line from the same ion but without this density sensitivity, a number of observational uncertainties cancel, making the method even more powerful. In addition, it has been shown that the ratio of emissivities for two optically-thin allowed transitions excited from the same level is dependent on temperature when the difference between the energies of the two transitions is of the order of kT (Heroux & Cohen, 1971). These ratios can thus be used as direct temperature diagnostics for the source plasma. A list of some diagnostic ratios and the density or temperature ranges over which they are useful is given in Table I.

SOHO is well suited to investigating the solar wind problem (Marsch, 1994). SUMER and its companion instrument, the CDS, will be able to diagnose plasma conditions, including flow velocities, in the inner corona, while the two onboard coronagraphs will provide information on conditions in the wind in both the subsonic and supersonic regions. This combined database will permit better maps of the solar wind flow to be made than ever before possible, and will permit a more detailed assessment of various theories for solar wind acceleration, for example, theories involving momentum transfer from Alfvén waves (Davila, 1985). These latter theories are particularly attractive for acceleration of high speed streams in coronal holes, since the magnetic field gradients in holes are small and it is known that, under these conditions, the dissipation length for Alfvén waves is very long (Wentzel, 1977). Thus, a gradual acceleration over very long distances becomes possible.

Of all the SOHO instruments only the SUMER spectrometer, measuring Doppler shifts and line broadenings with high spectral, hence velocity, resolution, will be able to estimate the energy fluxes at different heights or in various temperature layers ranging from chromospheric to coronal conditions. Combining these velocity measurements with local density and temperature determinations in fine-scale magnetic structures over this range of atmospheric conditions should provide us with the best data set yet obtained to assess mass, momentum and energy flux in the solar atmosphere and the heating of the corona.

2. The SUMER Instrument

The scientific objectives of the SUMER instrument call for observations in the extreme ultraviolet (EUV) from 500 to 1610 *Å*, where emission lines of atoms and ions in the temperature range of 10^4 to more than 2×10^6 *K* can be observed for examining the solar chromosphere, transition region and corona. We want to obtain dynamic and diagnostic information on the properties of the solar atmosphere, with an angular resolution of close to 1 *arcsec*, a temporal resolution of down to 1 *s* or even 60 *ms* for specific observations of intense lines, and a spectral resolving power of $\lambda/\Delta\lambda = 17700 - 38300$ ($\Delta\lambda \;\hat{=}$ pixel resolution element). Sub-pixel resolution must be achievable in the spectral regime compatible with the effective resolving power required for line-shift and line-broadening measurements.

2.1. TELESCOPE AND SPECTROMETER

The SUMER optical design is shown in Figure 2 and is based upon two parabolic mirrors, a plane mirror and a spherical concave grating, all made out of silicon carbide (Substrate: Reaction-bonded SiC; Surface: Chemical-vapour-deposited (CVD) SiC) and mounted in an aluminium housing which serves as the optical bench. The first off-axis telescope parabola, which has pointing and scan capabilities (the fastest rate is 300 *step* s^{-1} with 0.38 *arcsec* $step^{-1}$) of ±32 *arcmin* in two perpendicular directions, images the Sun into the spectrometer entrance slit plane. Pointing verification will be performed with the help of a Rear Slit Camera (RSC) operating in visible light (cf. Section 3.5. and Appendix A). The optical performance requirements led to a pointing mechanism design that approximates the motion of the telescope mirror around the focal point in the slit plane. The second off-axis parabola collimates the beam leaving the slit. This beam is then deflected by the plane mirror onto the grating. Two two-dimensional detectors, located in the focal plane of the grating and used alternatively, collect

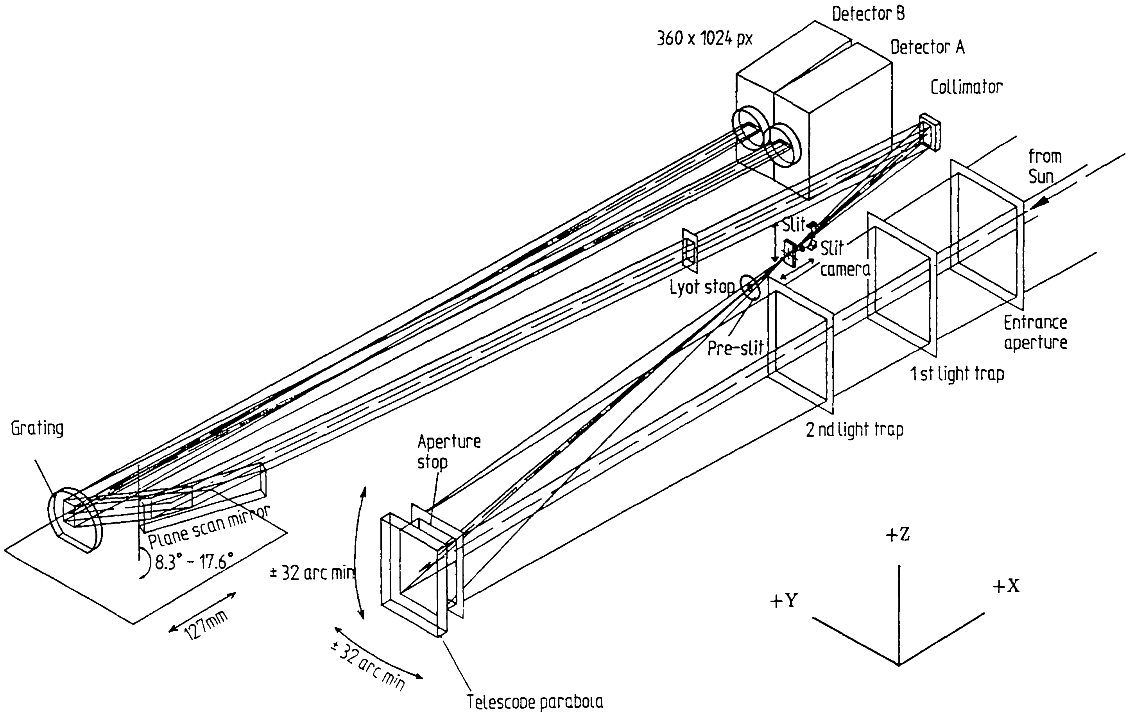

Fig. 2. The optical layout of the SUMER instrument showing the extreme rays as they propagate through the system. The ranges of movement of various mechanisms provided to control the positions of the optical components are indicated by arrows. The entrance door and its mechanism are not shown. An external alignment cube is available for spacecraft reference. Between the 1st and 2nd light trap, an electrostatic solar wind deflector is incorporated in the design to protect the telescope mirror from impinging solar wind protons. The spectrometer compartment is completely encapsulated in order to achieve good stray light performance and will only be illuminated through the slit engaged. Light-tight evacuation ports have been provided to facilitate pump down during test and launch. These ports are screened by a double potential barrier of ±18 V to prevent plasma from entering the spectrometer.

monochromatic stigmatic images of the slit in two spectral orders simultaneously. Coverage of the full spectral range requires a wavelength scan by rotating the plane mirror from 8.4° to 17.5° (with respect to the incident beam).

In order to establish the instantaneous wavelength coverage, we have to consider the detector and the photocathode geometry in Figure 3. A detailed description of the detectors will be deferred to Section 2.3.

The spectral resolution of the spectrometer can be deduced from the grating equation and the geometric configuration.

The angular location of a particular wavelength λ in the dispersion direction is given by the grating equation

$$m\lambda = d(sin\theta + sin\alpha) \qquad (1)$$

where m is the order, d is the grating spacing, θ is the angle of incidence on the grating and α is the angle of reflection off the grating. Note that θ

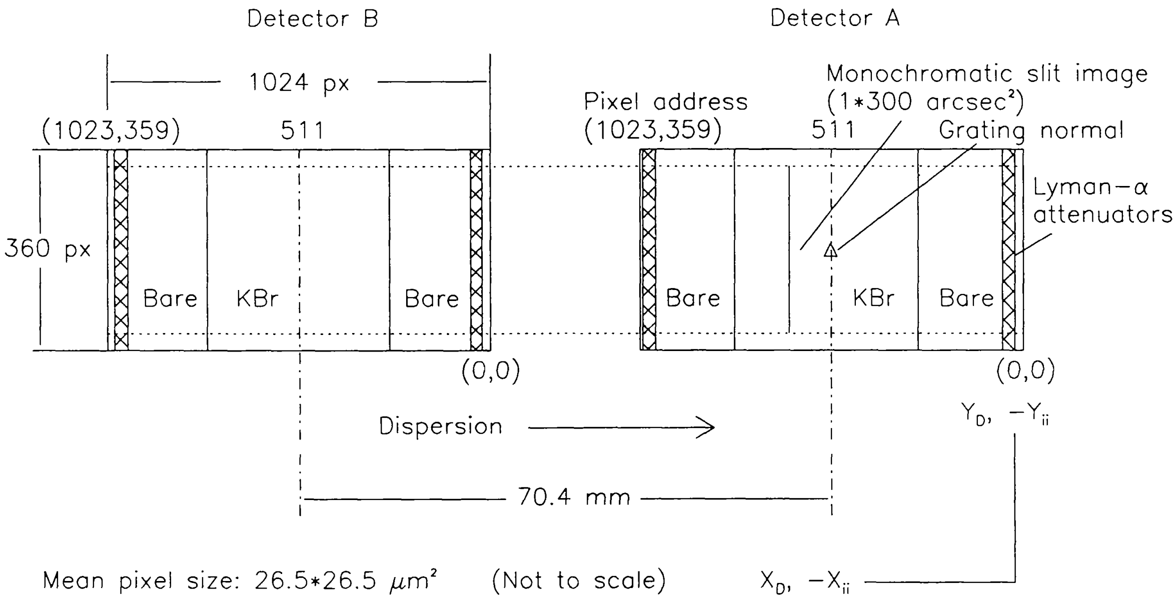

Fig. 3. Focal plane of the SUMER spectrometer showing both detector arrays. They are very similar as far as pixel and photocathode arrangements are concerned, but only detector A is centred on the grating normal with optimum optical performance in the Wadsworth mount. Detector B is offset by 70.4 *mm*. Only one detector can be switched on at a time. The Lyman-α attenuators consist of grids in front of the bare microchannel plates. Note that the slit image is shorter than the spatial extension of the detector. The "dark" pixels will be useful for scattered light measurements.

and α may have different signs. The order m is positive in the SUMER case. The actual radius of the spherical concave grating is $r_a = 3200.78\ mm$. The effective focal length of the grating depends on the angle of incidence (and thus on the wavelength) according to

$$f_\lambda = \frac{r_a}{1 + cos\theta} \tag{2}$$

Differentiating Equation (1) at constant θ and taking into account the geometrical configuration, we obtain an expression for the resolving power as a function of wavelength, namely,

$$\frac{\lambda}{\delta\lambda} = \frac{m f_\lambda \lambda}{d cos^3 \alpha \delta x} \tag{3}$$

where δx is the scale of resolution, usually given as the pixel size. It should be noted that the ideal Wadsworth mount requires $cos\alpha = 1$, which can, of course, only be satisfied for the centre of one detector. The centre of the other detector will be off the grating normal by a distance Δ resulting in

$$sin\alpha_B \approx \frac{\Delta}{f_\lambda} \tag{4}$$

With $\Delta = 70.4\ mm$ we obtain $cos\alpha_B \approx 0.999$.

Using Equation (3) we can determine the relationship between resolving power and wavelength for the SUMER grating. For our grating we have $d = 2777.45$ Å. With a 26.5-μm pixel size, we get a resolving power from 17700 to 38300.

Given a certain spectral resolution, the instantaneous wavelength coverage of the instrument is closely related to the detector dimensions. In Figure 4 we plot the instantaneous wavelength coverage of the detectors and the various photocathode regimes as a function of wavelength. For detector A it was assumed that the image of the slit in the reference wavelength λ_n was placed on the grating normal. Equation (1) thus reduces to

$$m\lambda_n = d\ sin\theta \qquad (5)$$

Incidence angles θ from 16.74° to 34.97° yield $\lambda_n = 800$ to 1592 Å in the 1st order and 400 to 796 Å in the 2nd order. The wavelength range, including the coverage provided by the detectors thus extends from 390 to 1610 Å. However, the use of the full range is severely restricted on the short-wavelength side by the fall-off of the reflectivity of SiC below 500 Å. At the long wavelength end, the range might be restricted by the total count-rate limitations of the detectors. It should be mentioned that both detectors will be illuminated simultaneously by the grating spectrum in 1st and 2nd orders. A change of detectors thus requires only detector power switching and no optical rearrangement. The resolution of the wavelength range adjustment for detector A is 0.28 Å per step at $\lambda_n = 800$ Å and 0.014 Å per step at $\lambda_n = 1597$ Å of the scan mirror mechanism. During actual measurements the scan mirror and, consequently, the grating focus mechanism remain static.

A sophisticated baffle system, consisting of an entrance aperture, light traps, an aperture stop (fixed in front of the moving telescope mirror and acting as a heat rejecting mirror for excess radiation), a pre-slit, a Lyot stop and various separating walls completes the design, whose basic characteristics are given in Table II. We note that the angular width of the 1-*arcsec* slits closely matches the detector pixel size that subtends between 0.95 and 1.03 *arcsec*. This slit width is also compatible with the optical performance of the telescope mirror (Wilhelm et al., 1994) as can be seen from Figure 5. This figure is based on evaluation of the telescope mirror measurements at the component levels and indicates a FWHM of the point spread function of 0.7 *arcsec*. The spectral resolution of the spectrometer is limited by the width of the slits and the size of the detector pixels. Note, however, that line shifts and broadenings can be determined with sub-pixel accuracy down to 0.1 *px* as has been demonstrated by simulation studies (see also Section 4.2.).

An important aspect of the optical system is the thermal control of the optical bench to a temperature range of $(20 \pm 1)°C$ during operation. This will be achieved by active thermal control supported by the good thermal

1995SoPh..162..189W

TABLE II

Basic optical characteristics of the SUMER normal-incidence telescope and spectrometer (1 *arcsec* at L1 corresponds to 715 *km* on the Sun).

The Telescope:	
Focal length	1302.77 mm @ 75 °C
Off-axis angle	4.5°
Equivalent f-number	10.67
Plate scale in slit plane	6.316 $\mu m\ arcsec^{-1}$
Total dynamic field-of-view	64 × 64 $arcmin^2$
Smallest step sizes (N-S and E-W)	0.38 $arcsec$
The Slits	1 × 300, 1 × 120, 0.3 × 120, 4 × 300 $arcsec^2$
The Rear-Slit Camera:	
Wavelength range	5770 – 6520 Å
Array size	512 (spatial) pixels
Pixel size	25 μm
The Spectrometer:	
Wavelength ranges	
Detector A	390 – 805 Å (2nd order)*
	780 – 1610 Å (1st order)
Detector B	330 – 750 Å (2nd order)*
	660 – 1500 Å (1st order)
Collimator focal length	399.60 mm
Off-axis angle	7°
Grating radius	3200.78 mm
Grating ruling	3600.42 $line\ mm^{-1}$
Magnification factor** in detector plane	4.092 at 800 Å 4.409 at 1600 Å
The Detectors:	
Array size	1024 (spectral) × 360 (spatial) pixels
Pixel size (mean value)	26.5 × 26.5 μm^2
Angular scale	1.03 $arcsec\ px^{-1}$ at 800 Å
	0.95 $arcsec\ px^{-1}$ at 1600 Å
Spectral scale	22.8 mÅ px^{-1} at 500 Å* (2nd order)
	20.9 mÅ px^{-1} at 800 Å
	45.0 mÅ px^{-1} at 800 Å (1st order)
	41.8 mÅ px^{-1} at 1600 Å

---

* In the range below 500 Å the sensitivity is very low, because of three normal-incidence reflections (cf. Figure 7). Strong lines have, however, been observed in this regime during the calibration phase.

** The magnification factor is the ratio of the effective grating focal length and the collimator focal length.

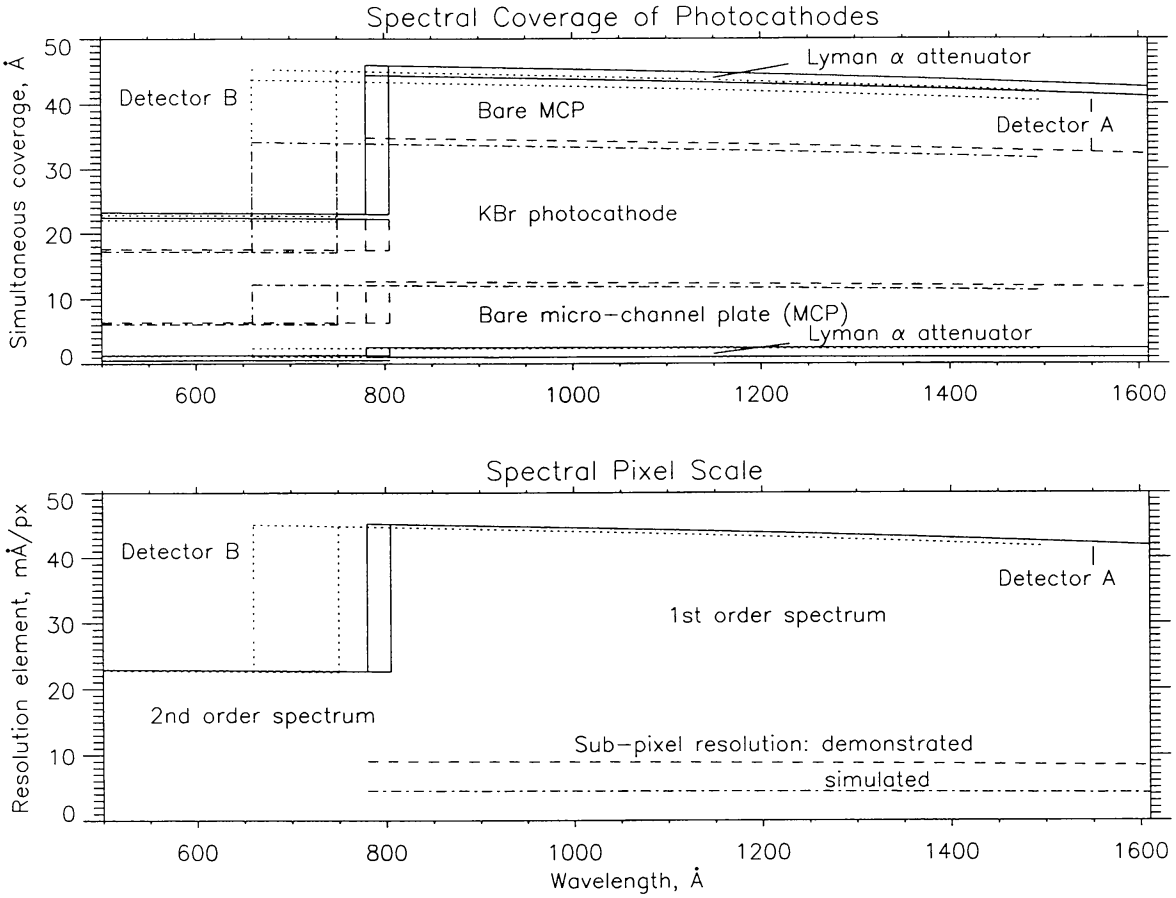

Fig. 4. Spectral coverage and resolution elements for various photocathodes or sensitive areas of both detectors. Also shown is the demonstrated and simulated sub-pixel resolution capability. Note that the ranges in first and second orders will be available simultaneously and that lines in the range from 660 to 805 can be observed in both orders.

conductivity of the aluminium housing and a multi-layer insulation (MLI). Most of the high solar power input into the telescope section, in particular, onto the telescope mirror, will be radiated to space by a radiator. The operating temperature of the telescope mirror will be 75°C. The SiC material has important properties in this context. The reflection in the visible is rather low (consequently the thermal input into the slit plane is not too high) and the thermal conductivity is good, avoiding large temperature gradients and allowing a radiative heat transfer from the mirror to its environment.

The SUMER telescope and spectrometer unit is isostatically mounted on SOHO with its boresight direction $(+X)$ fixed to within 8 *arcmin* of the SOHO fine Sun sensor reference. This, in turn, will be pointing towards the centre of the Sun with an accuracy of 10 *arcsec* and a stability of 1 *arcsec* (3 σ) over 15 *min*.

The SUMER flight software has been written under the assumption that the X-axis is pointing towards the Sun. Later, ESA defined an inter-instrument co-ordinate system (X_{ii}, Y_{ii}) with $+X_{ii}$ directed towards West and

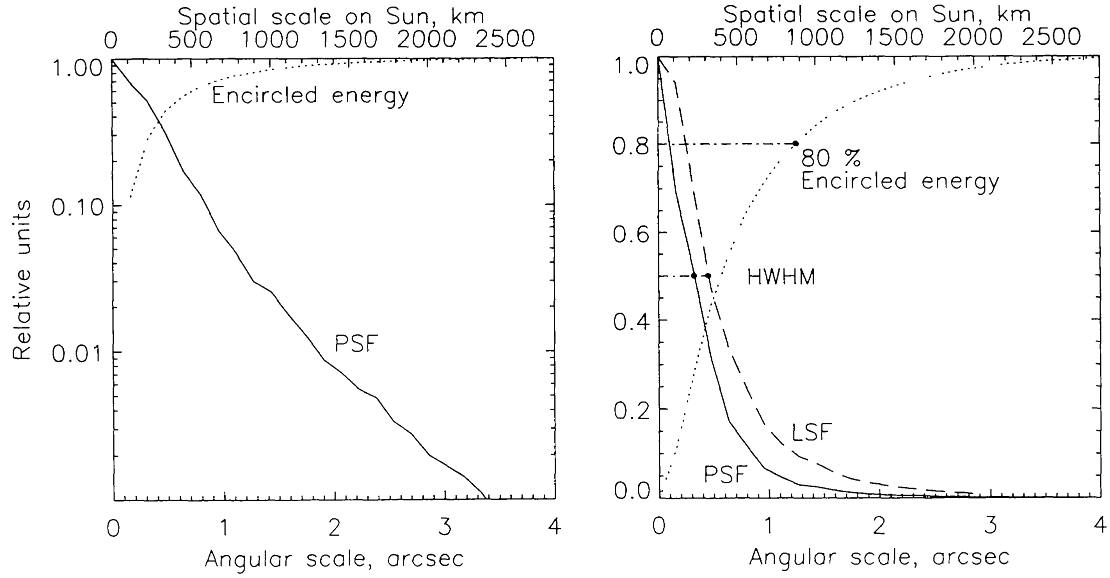

Fig. 5. SUMER telescope point spread (PSF) and line spread (LSF) functions in linear and logarithmic scales. Also shown are the encircled energy curves and the half-width at half maximum (HWHM) values.

$+Y_{ii}$ towards North (parallel to the projection of the solar rotation axis). We will use this system, when a spatial co-ordinate system is required, but – whenever the SUMER software is concerned – it should be noted that $Y_{ii} = -Z$ and $X_{ii} = +Y$ (with SOHO in its nominal attitude). The SUMER detectors require an additional co-ordinate system. The spatial direction will be defined by $Y_D = -Y_{ii}$ and the spectral direction by $X_D = -X_{ii}$. It is also worth pointing out that some of the units used in SUMER for the various axes appear to be unconventional. Their use was either dictated by hardware constraints or by the desire to limit the complexity of the onboard software as much as possible. In particular, we want to mention the smallest telescope step size of 0.38 *arcsec* and the point command unit of 0.0625 *arcsec*. In this contribution, we will avoid, if at all possible, SUMER specific units, but the user has to recognize that some of them will be of importance during the actual operation of SUMER.

2.2. CONTROL, TELEMETRY AND COMMAND SUB-SYSTEMS

In addition to the optical instrumentation, SUMER consists of two electronics support sub-systems, the Power Supply Unit (PSU) and the Digital Processing Unit (DPU). The motor control drive electronics for the various stepper motors of the mechanisms are decentralized and positioned close to the mechanism in question. All electrical systems are designed with a high level of functional redundancy.

An observation of solar events with SUMER will require a ground command or a command sequence to be sent to the instrument via SOHO. It should be assumed that the instrument is appropriately set up in a mode we will call "standby" here. Out of this mode all science programmes can be performed.

The primary output of the instrument will be image data of various formats. An image in the SUMER telemetry is an array of detector pixel intensities arranged in one spatial dimension along the slit and one spectral dimension in the dispersion direction. Each image is accompanied by an image header, which contains all the information relevant for evaluating the corresponding image. The header contains, in particular for each start of an exposure, the SOHO on-board time which is derived from the AIT (Atomic International Time) to correlate all SUMER images with other data sources. In addition, a housekeeping channel will transmit detailed information on the status of the instrument, but is not relevant in the context of this description. As the ultimate aim of the investigation is to obtain two-dimensional maps of solar areas in various spectral lines, the telescope scan capability perpendicular to the slit has to be utilized to construct these maps.

The nominal SUMER telemetry rate is 10.5 $kbit\ s^{-1}$. We will assume 10 $kbit\ s^{-1}$ to be available for science data and 500 $bit\ s^{-1}$ for housekeeping information. The rate can be increased to 21 $kbit\ s^{-1}$, if the CDS allocation is available for the SUMER instrument by special agreement. Alternatively, the SUMER rate can be given to EIT/LASCO (Delaboudinière et al., 1995; Brückner et al., 1995) for rapid transmission of reference images, or to CDS.

2.3. THE CROSS DELAY-LINE DETECTORS

Two cross delay-line detectors (XDL) are positioned in the focal plane of the SUMER spectrometer as shown in Figure 3. They are two-dimensional photon-counting, centroiding devices. The format is $27.0 \times 9.5\ mm^2$, electronically digitized to 1024 (spectral) × 360 (spatial) pixels each of approximately $26.5 \times 26.5\ \mu m^2$ in size. A low-resistance Z stack of microchannel plates (MCP) provides detection and amplification, and a multilayer, cross delay-line (XDL) anode accomplishes readout. The detector and its performance are described in detail by Siegmund et al. (1994).

Opaque KBr photocathode material is deposited on the MCP Z stack, selectively over the central half of the field of view. Incoming photons interact with the photocathode, resulting in photoelectron emission (Siegmund et al., 1987; Siegmund & Gaines, 1990) and a subsequent charge avalanche in the MCPs, giving an overall charge multiplication $\sim 2 \times 10^7$. This charge cloud is drifted from the MCP output to the delay-line anode. The charge is divided about equally between the XDL charge-collection fingers in the X_D and Y_D axes, which are connected to external serpentine delay lines (Siegmund et al., 1994). X_D and Y_D event centroid positions are deduced from the signal arrival-time differences at the two ends of each delay line. X_D corresponds to the spectral dimension and Y_D to the spatial one as defined above.

The KBr quantum detection efficiency (QDE) is $\sim$ 30% at 584 Å, $\sim$ 28% at 1066 Å, and $\sim$ 10% at 1360 Å. The bare MCP QDE is $\sim$ 8% at 584 Å, $\sim$ 5% at 1024 Å, and <1% at 1215 Å. Section 2.4., including Figure 7, provides further details.

The MCP photon-event pulse amplitude distributions are narrow, allowing amplitude discrimination of background events. The overall background rate is as expected for intrinsic beta-decay noise (Siegmund et al., 1988; Fraser et al., 1987) for K^{40} in the Philips MCP glass, with a rate of $<$ 1 $event\ cm^{-2}s^{-1}$ uniformly distributed across the field of view. Local-event counting rates in excess of 100 $event\ px^{-1}s^{-1}$ have been achieved with no degradation of the MCP gain. The event centroiding of the detectors is stable to better than 1 px for global counting rates up to $> 5 \times 10^5$ $event\ s^{-1}$. Detector electronic deadtime characteristics were measured, and were found to be < 40 % for counting rates up to 5×10^5 $event\ s^{-1}$. The count rate calibration carried out using the SUMER radiometric calibration source permits a deadtime correction to be applied with high accuracy when total count rates exceed $\sim 5 \times 10^4$ $event\ s^{-1}$. The thermal drift is < 1 px over the expected SUMER temperature range. Flat-field images are dominated by MCP fixed pattern noise and are stable. The MCP multifiber modulation is at a desirably low level (a few percent), nevertheless, an inflight flat-field correction can be applied to improve the uniformity of response further, if necessary. All basic detector performance calibration data are compiled into a "library" of detector functionality for the purposes of mission operations control, diagnostics and post-observation data processing.

Meshes with nominally 10% transmission are placed 9 mm in front of the MCPs at the extreme ends of their field-of-views (Figure 3) in order to cope with the intense Lyman-α line. The distance of 9 mm has been chosen to minimize the level of image modulation at 1216 Å resulting from the grid and the spacing. Electrostatic thermal ion deflectors are also placed in front of the detector aperture to prevent ions from striking the MCP. In addition, double-potential barriers screen all openings of the spectrometer compartment in order to repel thermal plasma particles.

A feature of the XDL system is a commandable artificial pulse (stimulation pulse) injected into each delay line at a rate of ~ 40 s^{-1}, resulting in a spot image effectively at the centre of the detector aperture. The data obtained from this feature give an in-orbit evaluation of the health of the detector electronics. In order to estimate the total counts collected in a certain area of the detectors, the DPU will keep a history memory of all counts and dump the information to the ground from time to time. It is thus possible to monitor all sections of the detectors irrespective of the science data selection method employed.

1995SoPh..162..189W

2.4. INSTRUMENT CHARACTERIZATION, RADIOMETRIC CALIBRATION AND CLEANLINESS ASPECTS

The optical characterization of SUMER was initially performed at the individual component and sub-system level, to verify the fabrication processes and performance of the optics. Characterization and radiometric calibration of the complete system were then carried out as follows; first, alignment and imaging tests were accomplished using visible light sources. Second, testing in vacuum with light sources above 1200 Å was performed to establish the performance and imaging quality in the VUV, and, third, measurements in the full wavelength range completed the calibration process. The tasks performed during the vacuum calibration included final optical alignment, calibration of mechanism transfer functions, verification of the telescope image quality, measurement of spectrometer resolution and contrast, stray light tests at all wavelengths and out-of-band suppression, wavelength and radiometric calibration.

The imaging properties of the instrument are verified using a light source which can fill the whole aperture of the instrument with a collimated beam. The system uses a collimator similar to the SUMER telescope mirror in order to provide a collimated beam of 150-*mm* diameter with high optical quality. As an example of the spectra obtained, we show in Figure 6 several Krypton lines on detectors A and B. For radiometric characterization, on the other hand, a calibrated light source as described below is used, which delivers a collimated beam that is not obstructed by any of the apertures of the SUMER instrument. From the known spectral radiation of the source and the recorded detector signal, the absolute spectral response of the instrument is determined.

The entire ranges of settings of all optical elements were examined with a view to uncover possible contributions of scattered light to the detector signals. When, during operations, the Sun is the target, Lyman-α radiation at 1216 Å in the zero and first order spectra will be by far the most significant contribution. Therefore, the scattered light measurements were carried out using a light source emitting two intense KrI lines at 1165 Å and 1236 Å close to the Lyman-α line. The counting rate of each of the "dark" pixels in Figure 3 near the lines due to scattered light was 2×10^{-9} of the total counting rate of the detector generated by the line signals. The average scatter contribution for all "dark" pixels was approximately 1×10^{-9} and less then 7×10^{-10} for spectral regimes outside the range from 1100 to 1300 Å. For bright active areas on the Sun, we expect an effective light input in Lyman-α that would correspond to 4×10^7 *count* s^{-1} for the 1×300-*arcsec*^{2} slit. We thus obtain a scattered-light contribution of 0.08 *count* px^{-1} s^{-1}, or 2.9×10^4 *count* s^{-1} for the full detector. This is well within the capabilities of the detector (4×10^5 *count* s^{-1} at 30 % loss). In this context, it should

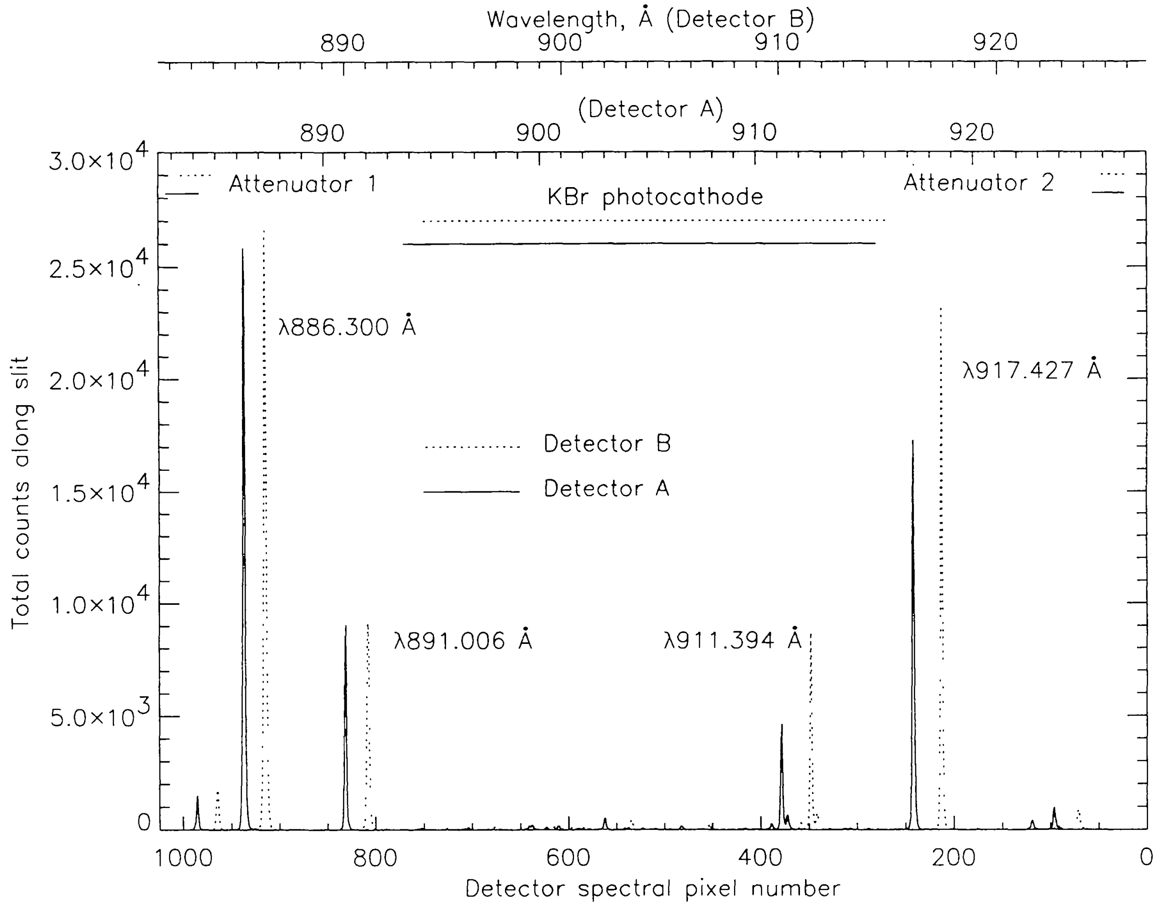

Fig. 6. Spatial pixel sums along the 1×300-$arcsec^2$ slit of two spectra taken with detectors A and B during the optical alignment tests with several Krypton lines near 900 Å. Also shown are the positions of the attenuators and the KBr photocathodes for detectors A and B. The wavelength scales of A and B are shown with an arbitrary offset of approximately 1 Å.

be noted that the application of the 0.3×120-$arcsec^2$ slit and an attenuator would allow us to observe the Lyman-α line even in bright active areas.

Schedule constraint did not permit measurements of the stray light characteristics of the flight instrument for off-band radiation at longer wavelengths. Theoretical considerations outlined below indicated that long wavelengths radiation should not contribute significantly to the detector count rate. Under the assumption that the scattering level of the grating is mainly due to small defects of the grating blank surface and to particles, the scattering follows a law proportional to $1/\lambda^2$. The diffraction tail measured at 1216 Å is 1×10^{-5}. With our assumption we extrapolated scattering values of 1×10^{-5} at 1000 Å, 6×10^{-6} at 2000 Å, 3×10^{-6} at 3000 Å, 1×10^{-6} at 4000 Å and, finally, 6×10^{-7} at 5000 Å. The quantum efficiency of the bare MCP has been measured at 2537 Å to be 6×10^{-6}. It is decreasing towards longer wavelengths and we assume here values of 1×10^{-6} at 3000 Å, 1×10^{-7} at 4000 Å and 1×10^{-8} at 5000 Å. The reflectivities of the SiC optical surfaces at long wavelengths are well known and have been taken into account when integrated spectra of the full Sun in 10 Å bands have been convolved with the scattered equivalent area of the instrument in the range from 1600 Å to 5000 Å. We obtain 5×10^{-5} $count\ px^{-1}s^{-1}$ or 18 $count\ s^{-1}$ for the whole detector. This level is totally negligible.

The stray light measurements have in the meantime been performed using a representative qualification model of SUMER. The measurements with a high-pressure Xenon lamp as radiation source have provided a good experimental estimate of the scattered light level induced by the long wavelength radiation. It has been found that it is below the background noise of the detector, i.e., below 1 $count\ s^{-1}$ for the whole detector.

The SUMER instrument is also sensitive to the state of polarization of the incident radiation primarily due to two optical elements, the plane mirror and the holographic grating. The angle of incidence of light striking the scan mirror varies from 72.5 to 81.6° (with respect to the mirror normal), which causes the mirror reflectance to depend on the state of polarization as well. Therefore, the measurement and characterization of this polarization sensitivity as a function of wavelength was performed using the engineering model optics (scan mirror and holographic grating) and synchrotron radiation, which is nearly 100 % linearly polarized, at the SUPERACO positron storage ring in Orsay. The polarization sensitivity or modulation factor of the SUMER instrument was found to be between 0.4 to 0.6, depending on the angle of incidence of the scan mirror, and will be discussed further in a future publication.

For the radiometric calibration in the entire wavelength range, a light source system had been developed using an open hollow cathode discharge lamp as the radiation source (Hollandt et al., 1993). The high-brightness lamp is mounted to an ultra-high vacuum system via differential pumping stages and a flux limiting aperture. A collimating, spherical concave mirror of 1090-mm focal length forms a collimated beam of 10-mm diameter. This mirror is tilted in horizontal and vertical directions, using bellows feedthroughs, in order to map the aperture area of the SUMER telescope. The system is mounted to the beam line of the SUMER test and calibration tank at a distance of approximately 6 m from the telescope mirror. The tilt angle can be compensated by the SUMER telescope pointing mechanisms in azimuth and elevation.

The plasma discharge source emits unpolarized line radiation at wavelengths given by the buffer gas used during a specific operation. For the spectral range of SUMER, the intense lines of the rare gases provide a good coverage of all wavelengths, and the resulting photon flux of the collimated beam, ranging from 10^7 to 10^9 $photon\ s^{-1}$ is suitable for the sensitivity of SUMER without exceeding the detector counting rate capability.

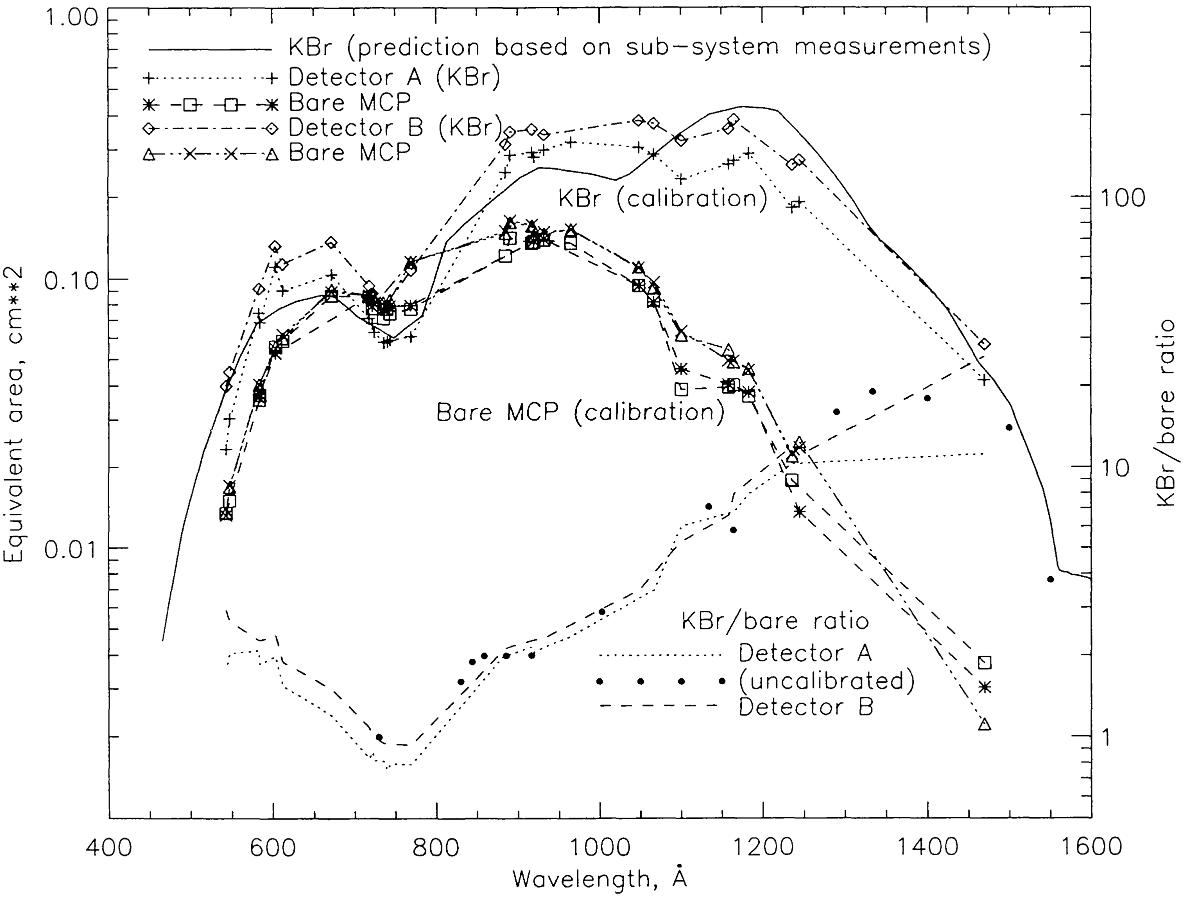

Fig. 7. The sensitivities of SUMER as obtained during the radiometric calibration are given in equivalent areas. Different curves are provided for detectors A and B as well as for each side of the bare microchannel plates and the KBr photocathodes. At the longest wavelength, only three bare sections have been calibrated. The KBr/bare ratios are also shown. In addition, this ratio (dots) was evaluated for detector A using uncalibrated lines in order to indicate its behaviour at long wavelengths.

The light source system has been converted to a transfer radiation source standard by comparing the emitted radiation flux with the spectral radiant flux of the BESSY electron storage ring, a primary standard. A total number of 32 emission lines have been calibrated between 537 Å and 1470 Å. By controlling the parameters of the discharge, the operation of the source can be kept stable and reproducible within better than ± 5 %. Consequently a resulting total uncertainty of less than 10 % (1 σ) of the absolute flux has been achieved. A similar system has been used for the radiometric calibration of CDS (Hollandt et al., 1993). First results of the radiometric calibration of SUMER are presented in Figure 7 for a central position of the light beam on the telescope mirror, but other areas of the telescope mirrors have been covered as well.

Concerning the detectors, note that both have central areas of KBr photocathodes which extend from pixel 280 to 770 for detector A and from pixel

270 to 758 for detector B. On either side of each KBr photocathode, sections of bare MCP are provided. In the original design, we tried to avoid bare sections of the MCP by applying a MgF_2 photocathode. This would have provided a substantial suppression of long-wavelength stray light contributions, but could not be implemented because of schedule constraints. The total sensitivity of SUMER is shown in Figure 7 as equivalent area in units of square centimetre. The maximum of the sensitivity is at approximately 1200 $Å$ with 0.4 cm^2 in good agreement with the performance prediction. Since the efficiency of the instrument is highest with the KBr portion of each detector at all wavelengths (in both 1st and 2nd orders), this is the area that will be used for most scientific studies. The other areas are provided for the following special purposes. For an unidentified spectral line, the ratio of its intensity as measured with KBr and with the bare parts of the MCP will establish whether it is being seen in 1st or 2nd order. Similar ratios will determine the various contributions to any feature that is a known blend of a 1st order line with one in 2nd order. Finally, the bare areas can be used to avoid saturation for very intense lines. The most extreme case, namely Lyman-α measurements in an active region or flare, will require the use of the attenuators. They reach from pixel 23 to 56 and from 982 to 1016 on detector A and from pixel 23 to 53 and from 970 to 1005 on detector B. By having these strips at both ends of the detector, either wing of Lyman-α can be selected during such observations. A detailed discussion of the radiometric calibration of SUMER will be given in a future publication.

The stability of the calibration during spacecraft integration, launch and operation is a concern. The normal-incidence optical scheme of the instrument and the aim to observe weak spectral lines in the presence of the full solar radiation impose severe demands on the requirements specifications for sensitivity and stray light. This renders the instrument very vulnerable to molecular and particulate contamination effects. In particular, the presence of both organic contaminants and UV radiation is known to produce irreversible deposition on the mirror surfaces by photochemical activation and subsequent polymerization. Prevention and control of contamination is thus a major effort and must be carried through the entire programme from the design phase to the end of the mission.

Many special features have been implemented in the design and fabrication of the instrument to reduce contamination including a very stringent material selection and cleaning programme. Contamination control has also been of major importance in the development and operation of the assembly area and of the calibration facility. Careful cleaning and vacuum baking was performed for every piece of flight hardware before entering the cleanroom. The cleanroom, which contains the assembly area, the optical alignment bench, and the calibration vacuum system, has been certified to Class 100 cleanliness. It contains an active charcoal filter panel in the air circulation system to clean the air from any condensable organic materials. The calibration vacuum system uses oil-free pumps only. The instrument can be inserted from the cleanroom side, while the vacuum support equipment is located outside the cleanroom. During ground handling tests and launch, the instrument will be protected by a door and a continuous dry nitrogen purge system. After launch the telescope mirror will be held at an elevated temperature with respect to the rest of the instrument. This will reduce chemical condensation on this critical surface. When the SUMER door is not open, the heating will be accomplished with the help of a window in the door not transparent in the UV range. During the transfer phase to L1, the door will be left partially open for several months in order to achieve efficient outgassing, yet without UV illumination of the telescope mirror. In this context, it should be noted that a co-ordinated calibration scheme with other instruments on SOHO has been worked out, and that rocket flights with calibration instrumentation will be extremely important.

3. Operating the SUMER Instrument

In the following sections, we describe the user interface which links the technical capabilities described so far to the scientific objectives we want to achieve. Thus, observers will get a deep, practical understanding of the instrument and a key how to handle it. Basic information is needed for both the features of the onboard command interpreter and programmes of the ground support equipment. The instrument will be communicating with a dual Electrical Ground Support Equipment (EGSE): a scientific EGSE which is based on a DEC ALPHA workstation, referenced here as operations station, and a PC-based maintenance EGSE. First, we briefly describe how the operation station will support the acquisition of science data. Then we focus on on-board features and describe the commands that control the instrument parameters of scientific interest, and explain the instrument characteristics related to the corresponding commands in enough detail for a successful observation.

3.1. SUMER GROUND-BASED COMMAND AND DATA SYSTEM

Two tasks have to be performed: telecommand management and telemetry management. SUMER commands will be sent by the ground station to SOHO and will be relayed to the instrument. The instrument will be operated either interactively, in batch mode or in time tag mode. Unless the instrument is operated interactively, the commands will be transmitted from the SUMER operations station to the spacecraft operations system long before the actual observation and will be dispatched to SOHO and SUMER. Batch operations or time tag operations will run sequentially. The batch command stack and the time tag command handler are both SUMER internal features. In interactive mode, the command authority will be granted to the SUMER operations station and all non-critical commands and/or verified command sequences will be relayed with minimum delay to the instrument. After completion of all jobs in a command queue, the instrument would go to its "standby mode". Although this is a safe configuration, no data would obviously be taken. In order to avoid long idle times in case of any interruption in the command link, the last job of any command uplink will be a "default mode", which will be activated 30 *min* after termination of the nominal observing session, if no new commands will have been received. The default sequence will engage the $0.3 \times 120\text{-}arcsec^2$ slit (to guarantee moderate counting rates under all circumstances, cf. 3.3.) and place it at Sun centre. The last reference pixel and wavelength called up in the previous sequence would be used and a 1024-pixel spectrum transmitted every 98 *s* (cf. Section 4 and Table V). The solar rotation provides the scan motion and thus no mechanism movements are required. This sequence could, in principle, continue for many weeks.

The operations station provides a telecommand generator which translates command sequences into machine readable form. Before application, command sequences have to be debugged, checked for parameter coherence and screened against erroneous or even dangereous contents. This is achieved by an instrument simulator which validates and verifies raw telecommand input. The simulator consists of two parts. The first one checks the effect of valid commands on all mechanisms and on the onboard 6-MB memory and the second photometric part determines the expected counting rates of the active detector as a function of the selected observing conditions. In addition to its debugging and safety functions the simulator has an administrative function, and is connected to the data base establishing a history log during the entire SOHO mission. Another link exists to a planning tool which is needed to implement individual observation programmes in the daily planning at the Experimenters' Operations Facility (EOF) at the Goddard Space Flight Center (GSFC) and to correlate studies among the SOHO coronal instruments and ground-based observatories. In addition, the parameters of observing sequences can be established and optimised with the help of an off-line programme which runs remotely and is available on request.

The operations station will receive the telemetry data stream related to SUMER. Real-time processes will store the raw telemetry packages, will separate housekeeping information from image information, and will display raw image data and pages of housekeeping data. A quicklook programme package is available for near-real-time image analysis. It receives data from the real-time processes and prepares them for a first assessment which includes image display, profile extraction, image calibration, geometric image correction, determination of dispersion and slit misalignment, image comparison and flexible image transport system (FITS) file generation. Its FITS file import/export capabilities make the data available for individual data analysis, for co-operative studies and for archiving purposes. Such activities will also be possible from MEDOC in Orsay.

3.2. SUMER Onboard Software

Operating the SUMER instrument is similar to operating an observatory. This requires an overall organizational strategy that allows us to perform both long-term planning and short-term fine tuning by parameter adjustments.

An analysis has shown that a short list of basic instrument functions complemented by features of any high-level computer language (e.g. loops, branches, mathematical library, relational operators) is sufficient to formulate even complex observational programmes. Consequently, a specific SUMER Command Language (SCL) has been developed for instrument operation which allows us to compile basic functions (sub-modes) on different levels of complexity into observational sequences.

Both Predefined Observational Programmes (POPs) and the option of User Defined Programmes (UDPs) will be available to the observer. POPs are complete observing sequences aimed at specific scientific subjects. They are resident in the flight software and can be executed by a single command, whereas UDPs have to be uplinked on demand at any time of operation prior to their execution. The SUMER Command Language has been used for POP definitions and will also allow the implementation of UDPs. It will also be helpful in managing operations. Small and capital letters are considered to be distinct characters by the SCL. A summary of the SCL is given in Table III, and some features are described in more detail in Sections 3.3. to 3.5. and 4.1. to 4.7. with emphasis on the imaging modes.

Normally, the instrument will be operated through this high-level command language. Only authorized people will have access to hardware-interfacing software modules which are not presented here.

3.3. Choosing the Proper Entrance Slit

At the focus of the SUMER telescope there is a slit assembly which has four different slits and a 1-*arcsec* diameter hole. Since the spectrometer is stigmatic, i.e. it does produce a focussed image of the slit on the detector, it can operate with a long slit to provide one spatial dimension. It is narrow in the direction of the wavelength dispersion to obtain good wavelength resolution. Spectroheliograms (called “maps” here) can be built up by scanning perpendicular to the long extension of the slit. Four slits are available as follows (cf. Table II):

A wide slit to improve counting statistics at the expense of spatial and spectral resolutions for observations off the limb is

TABLE III

High-level and library functions of the SUMER Command Language (SCL). Hardware interfacing functions are not listed here.

Observation Parameters	
slit(k)	binning($spec$, $spat$)
point(x, y)	compression(m)
rot_comp(Δt)	lambda{1,2}1(px, λ_1)
RSC(Δt)	lambda{1,2}3(px, $\lambda_1, \lambda_2, \lambda_3$)
sphel_mode(p)	lambda{1,2}8(px, $\lambda_1, \lambda_2, \lambda_3, \lambda_4, \lambda_5, \lambda_6, \lambda_7, \lambda_8$)
Mapping Modes	
RSC_scan(Δt, Δx, n_s)	spectrohelio{1,2,3,4}(Δt, f, Δx, n)
expl_event_search(Δt, f, Δx, n, lev, t_{min}, t_{max})	full_disk(Δt, f, Δx, $schm$, $centr$)
celestial_obj(t_{max}, t_{stp}, n_{img}, $dark$, λ, Δ, n_{inc})	ref_spec(Δt, f, λ, $\Delta\lambda$, n_{inc})
Special Functions	
AFT(); abbreviated functional test	FlatField(Δt, λ, f_1, f_0)
cont(); IIF flag or repoint check	IIM_mode(m); image integration memory mode
contY()*; solar E-W coordinate	IIM_div(div); division in image memory
contZ()*; solar N-S coordinate	Set_SphelDirection(dir)
FF_mode(m); flat-field correction	Set_SphelPointCenter(x, y)
flag(x, y, ev); IIF message	
Library Functions	
abs(x); absolute value of integer	log10(x)
atan(x)	Param{R,S,U}(nr)
atan2(y, x)	pow(x, y); x^y
ceil(x); smallest $i \geq x$	PutPixel{B1,B2,I2,R4}(nr_{ch}, ch, $zpos$, val)
cos(x)	
exp(x)	PutSystem{R,S,U}(nr, val)
fabs(x); $\|x\|$ for floating point number	SendImage(f)
FilesInRAMDisk()	sin(x)
floor(x); largest $i \leq x$	sqrt(x)
fmod(x, y); x mod y	System{R,S,U}(nr)
GetImageMax()	tan(x)
GetPixelB2(nr_{ch}, ch, $zpos$)	Wait(Δt)
log(x)	WaitImage()

Note: {a,b,c} means choice of either a, b, or c.
* Note definition of coordinate system

Slit 1 with dimensions corresponding to 4 × 300 $arcsec^2$. This slit must not be used for on-the-disk observations.

The standard slit tailored to achieve the best possible spectral and spatial resolution figures is

$$\text{Slit 2 with } 1 \times 300 \; arcsec^2.$$

For intense lines,

$$\text{Slit 4 with } 1 \times 120 \; arcsec^2$$

can be used, and finally, a short, narrow slit for very intense lines or high continuum regimes is available as

$$\text{Slit 7 with } 0.3 \times 120 \; arcsec^2.$$

The use of the slits will be determined by the observational conditions. For normal line intensities and low continuum regimes, slit 2 will be preferable, as it provides maps of larger solar areas in a given time span than the shorter slits. Shorter slits will decrease the continuum contribution to the total counting rate, and the narrow slit will attenuate both the lines and the continuum.

All slits will be parallel to the CDS normal-incident slits and will extend in the solar North-South direction, when SOHO is in its nominal attitude. A change in slit orientation will require a roll manoeuvre of SOHO. The slit selection will be performed by the command

"slit k"

where $k = 1, 2, 4$ or 7.

The slits will be centred on the spatial dimension of the detectors. For a wavelength of 1600 *Å* in first order, the magnification factor attains a maximum of 4.409. Thus, the long slits length (of 1.89 *mm*) will give an image length on the detector of 8.35 *mm*, or 315 *px*. The dark pixels of the detector on either end are extremely important for assessing the scatter characteristics of the spectrometer, but are also facilitating the alignment of the instrument. The slit selection mechanism will allow us to adjust the slit image position on the detector in steps of 1 *arcsec*. Together with a history memory, this adjustment of the short slits could be used to achieve a uniform detector ageing. It should, however, be noted that only people with system authorization will be able to use the fine adjustment of the slit position.

A user can, however, position the short slits off the centre by commanding

"slit k"

where	$k = 3$	for slit 4 in bottom position (small spatial pixel numbers)
	$k = 5$	for slit 4 in top position
	$k = 6$	for slit 7 in bottom position
and	$k = 8$	for slit 7 in top position.

In bottom position, approximately one third of the short slits will be obscured by a baffle behind the slit plane. The small hole can be engaged by "slit 9" and might be useful for specific investigations. A slit focus mechanism is also available, but its operation is restricted to authorized SUMER personnel. Scientists noting an apparent degradation in focus quality are thus requested to document the evidence and to contact the SUMER team member on duty.

3.4. POINTING THE SUMER TELESCOPE

The observation of a specific solar feature or event requires the telescope to point in the desired direction. Through in-flight calibration, the SUMER internal co-ordinate system will be adjusted to the SOHO co-ordinate system. The command to direct the telescope to a certain direction is

"point x y"

where $+x$ is towards West and $+y$ towards South. Note that the actual pointing will be performed in steps of 0.38 *arcsec* and that the internal transmission time for each point command is 90 *ms*. This command will point the centre of the slit selected to the corresponding solar co-ordinates. As was mentioned earlier, the mechanical range of the point capability is ± 32 *arcmin* in x and y, of which 8 *arcmin* might be needed for the initial SUMER/SOHO alignment. Consequently, ± 24 *arcmin* are routinely available for pointing. This range is in line with the predicted scatter performance of the SUMER telescope, which will allow us to observe intense lines up to 8 *arcmin* above the solar limb or 1.5 $R_\odot$ (solar radii) from the centre.

Small-scale observations over an extended period of time will require a compensation of the solar rotation. SUMER provides a function to do this. By commanding

"rot_comp 0.0"

the standard rotation compensation is selected, where the compensation value depends on the current pointing x, y. Details on the standard compensation scheme are described in Appendix B.

If the standard compensation is not adequate for the observation in question, the user can select her/his own compensation scheme and set the compensation interval by commanding

"rot_comp Δt"

where $\Delta t > 0$ is the time period (in seconds) after which a 0.76-*arcsec* correction step will be performed. For $\Delta t < 0$ the compensation is switched off. The standard correction will be performed whenever one of the image acquisition functions (spectroheliol, 2, 3, 4 and ref_spec) to be described later is called and will be updated whenever a new mapping sequence is initiated. During long observation sequences of small-scale events, the SUMER telescope will thus follow the event with an accuracy provided by the differential rotation approximation. It should be noted that the update process is not available within one observation sequence if the user has selected a specific compensation scheme. For short-term observations this probably will be acceptable, but not for long duration monitoring.

3.5. THE REAR SLIT CAMERA (RSC)

The main purpose of the rear slit camera will be the pointing verification of the SUMER telescope by observing the diffracted, visible light behind the slit (for details see Appendix A). Both solar limb determinations and sunspot observations will be possible.

For electrical and thermal reasons, the RSC is normally switched off when SUMER is in "standby mode". With

"RSC Δt"

a user can switch on the camera and read out a single, one-dimensional image of 512 *px* oriented along the slit at the current telescope pointing position with an integration time parameter $\Delta t = 0, 1, 2, 3$ corresponding to 77, 103, 155 or 206 *ms*. The command

"RSC_scan Δt Δx n_s"

switches on the RSC and acquires n_s groups of 50 RSC images starting at the current telescope pointing position and stepping the telescope azimuth mechanism by $50 \times n_s$ increments Δx (in units of 0.38 *arcsec*) perpendicular to the slit from East to West if Δx is positive and in the opposite direction if Δx is negative.

4. Constructing a SUMER Observing Programme

4.1. PREPARING FOR AN OBSERVATION

In preparing for an observation the user has to decide beforehand on some parameters and dispatch the appropriate commands. Among those

"sphel_mode p"

controls whether multiple-phase observations will switch from one phase to the next upon receipt of an Inter-Instrument Flag (IIF) or a repointing command. If p=0 the observation will be continued, for p=1 an IIF will terminate the current observation and initiate the next phase and for p=2 a repointing command will lead to a corresponding action. The command p=3 should be set, if both events should trigger such a change. With p set to 2 or 3, the observer has a powerful tool for controlling batch runs with interactive point commands.

The next two commands are intimately related to the scientific requirements and the limited telemetry available for SUMER. In principle, SUMER could produce measurements in every second or less over the full detector area of 1024 spectral by 360 spatial pixels with 16-bit resolution corresponding to a data rate of more than 5.9 $Mbit\ s^{-1}$. This value has to be compared with the telemetry rate available to determine if data selection, reduction, and compression schemes are compatible. We will defer the data selection aspects to later sections and discuss here the SCL function

"binning *spec spat*"

as a typical data reduction method. The parameter *spec* controls binning of the 1024 spectral pixels and *spat* that of the 360 spatial pixels. Not all combinations will produce data formats compliant with the existing telemetry and compression schemes (for details see following sections and also Table V). No binning is set by default or can be selected by

"binning 1 1".

While binning leads to an unrecoverable loss of information, the compression methods to be discussed next aim at a more or less complete recovery of the original information by the application of decompression algorithms on the ground. The command

"compression m"

with $m = 1, 2, \ldots\ldots 17$ selects a specific scheme to compress the SUMER image data prior to transmission. Whether the image data will be compressed at all will be determined by the image format requested in an imaging function (cf. Section 6.3), i.e., if an uncompressed data format is chosen then no compression will be performed.

If the parameter m is set to 0, no automatic compression and transmission will be done and the user has the option of implementing a user defined compression. If the parameter m is set to a negative value, in addition to the user defined compression, an automatic compression defined by $|m|$ will be executed after the image has been released to the telemetry. Note that the user defined schemes can only be applied to single images and require a specific release action per images.

Table IV lists the parameter values m for the compression schemes available and the corresponding compression execution times in the SUMER DPU. The execution times are calculated for the compression of an image of 16-bit raw data with 50 pixels in spectral and 360 pixels in spatial direction, but the schemes 1 to 5 can be applied to any input format and the schemes 6 to 16 also work for 120 spatial pixels. The Gaussian fits determine and transmit up to three statistical parameters (maximum, centroid, width) and the background. The A schemes provide the exact maxima, but may underestimate the intensity, while the B schemes give the correct intensity (cf. Dammasch, 1992). For compression scheme 17, three such images taken from the same integration are extracted for compression. The times are valid for the nominal SUMER DPU system configuration where both the Experiment Control Processor (ECP) and the Signal Processing Unit (SPU) are active. In an emergency configuration where only one of them is operational, the compression times will be higher by at least a factor of 2. Before binning or compression schemes will be activated, the user can consider the application of a detector flat-field correction.

TABLE IV

Onboard compression schemes and their execution times for an input format of 50 (spectral) × 360 (spatial) pixels (2B).

Parameter m	Compression Scheme	Time, s	Output format
1	Bytescale (Min, max)	0.69	50 × 360 (1B)
2	Bytescale (Local-high)	0.89	50 × 360 (1B)
3	Squareroot (Min, max)	1.15	50 × 360 (1B)
4	Squareroot (Local-high)	1.35	50 × 360 (1B)
5	Quasilog (Min, max)	0.92	50 × 360 (1B)
6	Relevant (Squareroot, max)	8.28	25 × 360 (1B)
7	Gauss (A1)	1.03	1 × 360 (2B)
8	Gauss (A2)	1.03	2 × 360 (2B)
9	Gauss (A4)	1.03	4 × 360 (2B)
10	Gauss (B1)	0.96	1 × 360 (2B)
11	Gauss (B2)	0.96	2 × 360 (2B)
12	Gauss (B4)	0.96	4 × 360 (2B)
13	Prim_1 (Fast fit)	0.63	1 × 360 (2B)
14	Prim_2	0.69	2 × 360 (2B)
15	Prim_4	0.77	4 × 360 (2B)
16	Addition scheme	0.29	1 × 360 (2B)
17	5 statistical moments of 3 lines	0.84	5 × 360 (1B)

4.2. EMISSION LINE SELECTION

The process of data selection is intimately connected with scientific considerations as to which solar emission lines are needed for the desired investigation. In principle, the user is free to select any line in the wavelength range from approximately 500 to 1610 Å or any combination of lines. It should, however, be noted that there are severe operational constraints. To run SUMER efficiently the user therefore has to understand the wavelength setting in some detail. The most important aspect is that only two bands can be observed simultaneously on one of the detectors. Their widths are approximately 44 Å in first order and 22 Å in second order (see Figure 1 and Section 4). A diagram of the focal plane geometry of the spectrometer has been shown in Figure 4. Only one of the detectors A and B will be activated at a time. Under normal operational conditions this will be detector A. Should the detector B have to be selected by the SUMER operational team, the user interface will not change, but the available wavelength range will be different due to the offset in position of detector B with respect to detector A. Note, however, that the grating normal of the Wadsworth mount

1995SoPh..162..189W

is centred on detector A. It is possible, if needed, to select either the best spectral focus or the best spatial focus on detector B.

It is further of importance to realize that the Wadsworth mount requires a focal length adjustment of the grating/detector configuration whenever the wavelength range is changed. Consequently, any change in the wavelength range leads to activations of two mechanisms: (1) the scan mirror mechanism in order to change the angle of incidence on the grating and (2) the grating focus mechanism in order to adjust the grating/detector distance according to the effective focal length of the grating. SOHO attitude constraints required the implementation of a ramping scheme for the SUMER grating focus mechanism leading to a time delay of more than 20 *s* for a scan over the full wavelength range. For some line combinations, the different wavelength ranges of the detectors A and B could be utilized to minimize the scan times. In Table I, for instance, the N IV pair at 923/765 Å can only be accommodated on detector A close to its extreme limits, whereas it can be obtained in 1st order in close vicinity on detector B. Another penalty in using substantial wavelength changes is the wearing out of the mechanisms. Mechanism activation times will be a controlled resource during the mission. The allocation will be based on lifetime predictions and run time history logs.

In short, the ideal observing programme does not require changes of the wavelength range and all long-wavelength lines are positioned on the KBr photocathode, and Lyman-α, if observed, is on the attenuator. This is easy to perform for any observation involving only one line. In this case the command

“lambda11 px λ_1”

will position the line with wavelength λ_1 (in Å) on the spectral pixel address px. See Figure 4 for a first idea on the pixel address. For instance, $px = 511$ would be the centre of the detector A (or B). If three lines have to be observed in one wavelength range the command

“lambda13 px λ_1 λ_2 λ_3”

will again put line λ_1 on px and, in addition, will determine the resulting positions of wavelengths λ_2 and λ_3 in spectral pixel units for data selection. Similarly

“lambda18 px λ_1 λ_2 ... λ_8”

does the job for up to 8 lines. Values of 0.0 must be inserted for unused parameter slots. The SUMER ground support equipment will perform a check whether or not all lines will be imaged on the detector. The lambda functions will take care both of the scan mirror mechanism and the grating focus mechanisms settings.

For many line ratio observations or other investigations, the ideal situation will not be achievable. In this case the SCL provides the facility to define alternate line registers by lambda21, lambda23 and lambda28 which will be called by observing programmes when needed.

The process of line selection might be demonstrated with the help of Figure 8 which shows in the upper two panels lines on KBr in the complete spectral range of SUMER in 1st order (on detectors A and B) and superimposed the 2nd order lines. The spectrum was obtained during the SUMER alignment activity with a windowless Krypton lamp. In the third panel, part of the spectrum of detector A is repeated showing the different responses of the KBr photocathode and the bare MCP to long-wavelength radiation. With 1024 spectral pixels, this panel corresponds to a single detector exposure. In the bottom panel finally, two Pt lines are depicted to demonstrate the resolution capability of the instrument. In the solar spectrum the Doppler widths of lines, given by

$$\Delta\lambda_D = \frac{\lambda}{c}\sqrt{\frac{2kT_i}{m_i} + \delta v^2} \tag{6}$$

where λ is the wavelength, c the velocity of light, k the Boltzmann constant, T_i the ion temperature and m_i the ion mass and δv the random motion amplitude, are typically 120–200 $m\AA$ or 3 to 10 detector pixels. The instrumental influence is shown to be smaller than that. To cover a line in the spectral domain normally requires about 25 pixels and in special cases 50 pixels. Data selection will consequently be performed by extracting windows of 25 or 50 spectral pixels centred around the lines of interest. It should be mentioned that a major performance characteristic of SUMER, namely to measure line shifts and widths with sub-pixel accuracy (cf. Section 2.), could be verified during the alignment test. It was found that a line shift could be identified down to 0.2 of a pixel. This value is, however, a convolution of the detector resolution and the scan mirror encoder resolution used for measuring the offset in the laboratory. Consequently, we can expect a better performance of the detector alone when observing solar line shifts.

4.3. MAKING SPECTROHELIOGRAMS

We are now in a position to describe the actual mapping of solar areas. The basic process is the stepping of the slit in a direction perpendicular to its long extension while detector images are being exposed and relevant spectral information is being extracted. It can be controlled by commanding

“spectroheliol Δt f Δx n”

The function spectroheliol acquires up to eight spectroheliograms simultaneously with integration times indicated by Δt (values > 0 give the time in units of 250 ms, a value of 0 sets the integration time to 60 ms). The wavelengths to be used are those entered in the latest call to one of the modules lambda11, lambda13, and lambda18, i.e. the pixel locations are taken from the main line register. The image format for the transmission of the

1995SoPh..162..189W

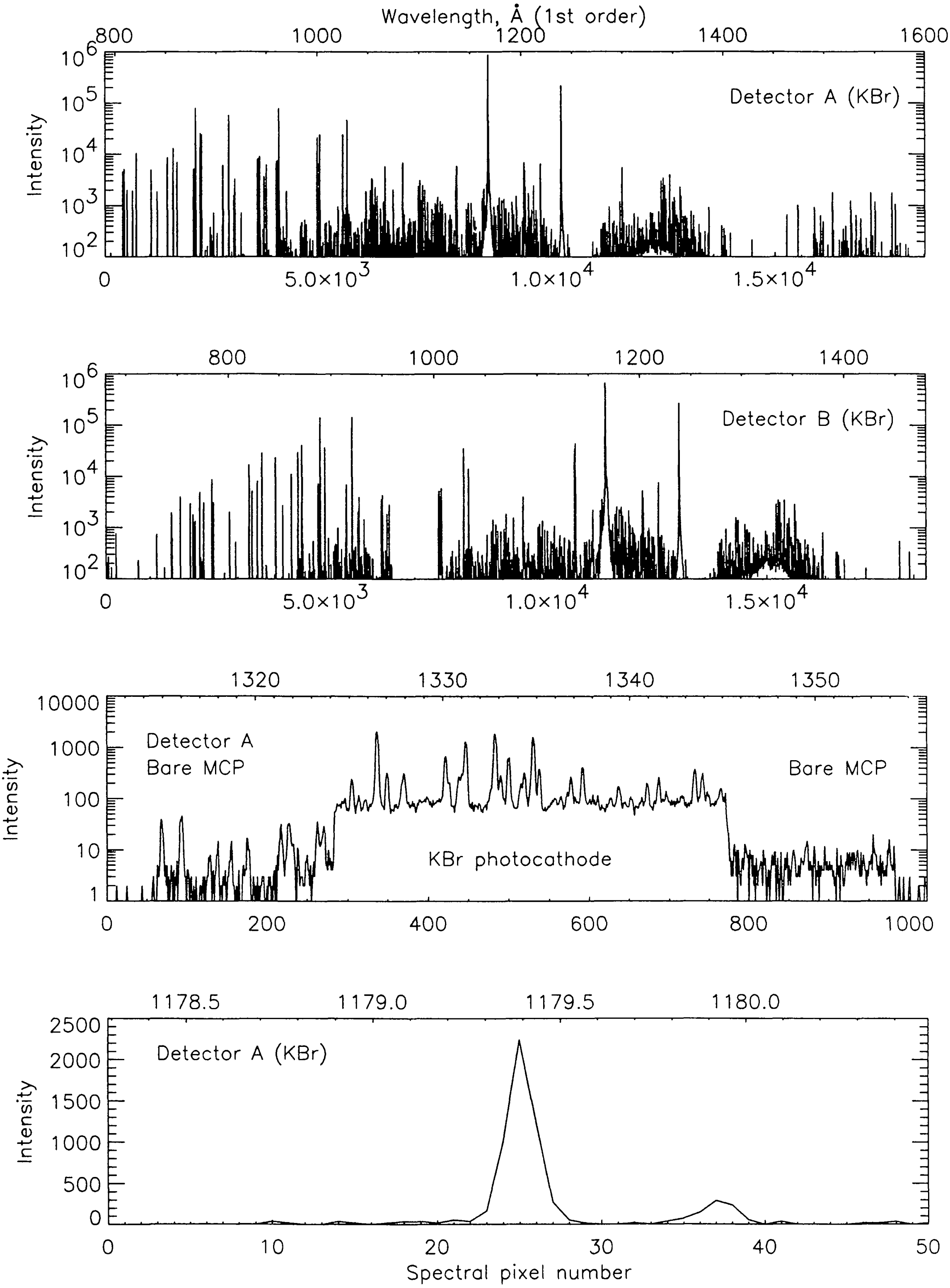

Fig. 8. 1st and 2nd order spectra of an open Krypton lamp measured during the SUMER alignment activities with detectors A and B on the KBr photocathodes (upper two panels). Note the different wavelength ranges for detectors A and B. The lamp was off for some time during the exposure of the spectrum on detector B (~ 900 to 1000 Å). Krypton spectrum near 1330 Å showing all spectral pixels of detector A (3rd panel) and high-resolution spectrum (bottom panel) of a Pt-Ne hollow cathode source. The wavelength in Å is given for the first order on top of each panel. Below we show the spectral pixel number.

image data is given by f. Taking the SUMER spectrometer and detector design into account, a limited number of image formats have been defined. A selection of formats is listed in Table V.

TABLE V

Image formats, data reduction options, compression schemes and transmission times at 10 *kbit/s*.

Uncompressed Data			Maximum binning		Compressed Data			
Format	Size	Time			Format	Size	Time	Scheme
f	*spec spat*	*s*	*spec*	*spat*	*f*	*spec spat*	*s*	number
3	1024×360	590	1	1	2	1024×360	295	1 .. 5
5	1024×120	197	1	3	4	1024×120	98	1 .. 5
9	50×360	28.8	20	1	8	50×360	14.4	1 .. 5
					12	25×360	7.2	6
11	50×120	9.6	20	3	10	50×120	4.8	1 .. 5
					14	25×360	2.4	6
13	25×360	14.4	40	1	12	25×120	7.2	1 .. 5
15	25×120	4.8	40	3	14	25×120	2.4	1 .. 5
37	256×360	148	4	1				
39	512×360	295	2	1	38	512×360	147	1 .. 5
			1	30	40	1024× 12	19.6	1 .. 5
			20	1	18	1×360	0.6	7,10,13,16
			20	3	20	1×120	0.2	7,10,13,16
			40	15	30	25× 24	0.5	1 .. 5
			20	15	31	50× 24	1.0	1 .. 5
			20	1	41	2×360	1.2	8,11,14
			20	3	42	2×120	0.4	8,11,14
			20	1	43	4×360	2.3	9,12,15
			20	3	44	4×120	0.8	9,12,15
			1	1	45	5×360	1.4	17

The original data have 2 bytes and the transmission time is given under the assumption of a 10 *kbit* s^{-1} science telemetry rate. The transmitted image formats are, however, not necessarily original data formats, but could have been reduced by certain binning operations. The maximum binning parameters compatible with both the detector array size of 1024 × 360 and the telemetry format are indicated as well. On the right-hand side, image formats are listed which are available after data compression operations. Compression schemes 1 to 6 and 17 will lead to 1 byte integer values, and schemes 7 to 16 will output 16 bit integer values.

The parameter n gives the number of steps of a step size Δx (in units of 0.38 *arcsec*) each to be performed by the telescope pointing mechanism.

The number of images acquired is therefore $n + 1$. If the parameter n is positive, the telescope is stepped in the $+x$ direction (East to West); if n is negative, stepping is in the $-x$ direction (West to East); if n is zero, no stepping is performed, i.e. a single image is acquired.

If the parameter Δx is positive, it indicates the step size. If Δx is negative, a special operation mode ("smear step") is activated, where the pointing is stepped $|\Delta x|$ times by one elementary step of 0.38 *arcsec* per integration interval. The speed is limited by the internal point command time mentioned in Section 3.4. If $\Delta x = 0$ then $n + 1$ images will be taken at a fix pointing position.

The field-of-view of the spectroheliograms results from the length of the slit and the scanning motion of the telescope mirror of n steps with an incremental step width of Δx each. Given the solar co-ordinates (x, y) the telescope is currently pointing to and the length l of the slit selected, the field scanned is represented by the rectangle ($x \pm |n \times \Delta x|/2$, $y \pm l/2$). This geometry can easily be described by saying that the scan range mapped by the instrument is centred on the pointing direction.

After the scanning has ended, the pointing is returned to the initial position. The command

"spectrohelio2 Δt f Δx n"

is very similar to spectrohelio1 with the exception that it uses the lines stored by lambda1 and lambda2 alternatively. It is thus specifically designed for line ratio observations with lines too far apart to be covered with a single wavelength setting. Spectrohelio2 is unable to perform "smear steps".

Spectrohelio1 and 2 both do not affect the current pointing. However, they do, unfortunately, exercise the telescope azimuth mechanism more than is required by the mapping process. If multiple mapping of the same solar region is part of the observing programme, it is therefore advisable to step the telescope forwards and backwards alternatively. This can be done with

"spectrohelio3 Δt f Δx n"

and

"spectrohelio4 Δt f Δx n"

in analogy to the modes 1 and 2.

4.4. COMPLEX MAPPING MODULES

The command

"full_disk Δt f Δx *schm centr*"

will lead to the acquisition of a huge spectroheliogram covering either the whole solar disk (*centr* = 0) or the neighbourhood (±2 *arcmin*) of the central meridian (*centr* = 1). As for the spectrohelio modes, Δt determines the integration time per exposure, the image format can be selected by f and Δx gives the step width during the mapping. If *schm* is set to a negative value the steps will be performed in "smear step" mode. The full_disk module

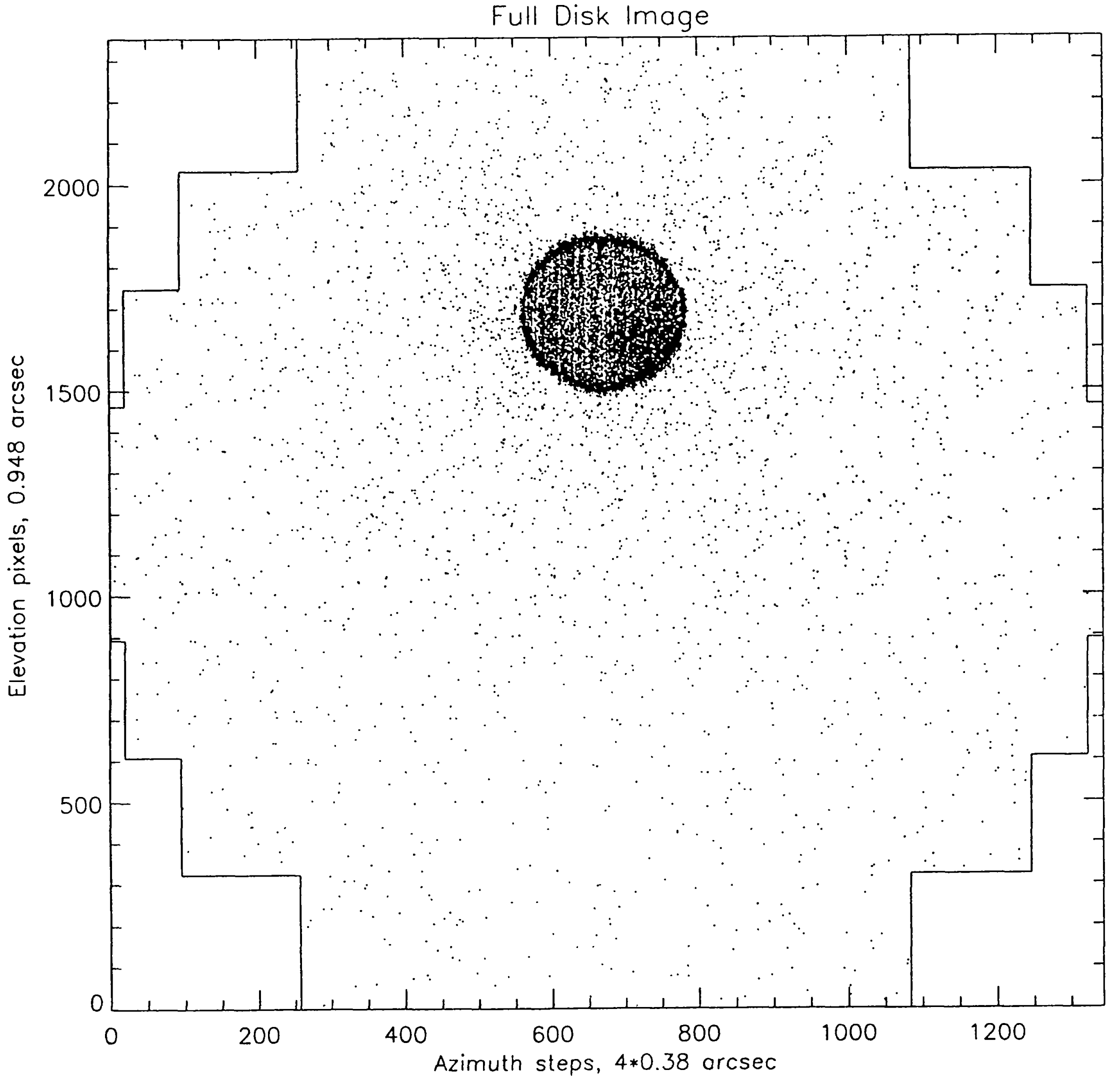

Fig. 9. Map of the SUMER alignment lamp aperture and its surrounding scanned with the help fo the "full-disk" module (line KrI λ 1164.9 Å). The scatter is mainly determined by the illuminating collimator and is not related to the SUMER optics.

produces large maps, such as shown in Figure 9 for the aperture of the SUMER alignment lamp in KrI (λ 1164.9 Å). With a step width of 4 × 0.38 *arcsec* and an integration time of 2 *s*, the run time was 5 *h* 53 *min*.

The command

"expl_event_search Δt f Δx n lev t_{min} t_{max}"

looks for explosive events on the Sun in a field-of-view that is represented by the rectangle $(y \pm n * \Delta x/2, z \pm m/2)$ where (y, z) are the solar co-ordinates of the current telescope pointing and m is the length of the slit used. The integration time is indicated by Δt (cf. spectroheliol) and the image format is f. The search starts after the minimum time t_{min} (in units of 250 *ms*), it ends after the maximum time t_{max} (in units of 250 *ms*). In the search phase, the instrument determines line shifts of a line that will have to be identified by lambda11. If an event exceeding the threshold *lev* is detected within the defined time span, an inter-instrument flag is issued providing the solar co-ordinates of the event to other instruments. In addition, the telescope pointing is adjusted so as to position the event on the centre of the slit. In the search phase, images will be acquired and stored until the minimum time t_{min} is reached. After that, the oldest image will be overwritten by the latest image until the maximum time t_{max} has been reached. During the study phase any lambda function and spectrohelio mode can be selected. In order to allow very high-temporal resolution observations of small-scale events, windows of 24 spatial pixels have been defined for this application.

With the command

“ref_spec Δt f λ $\Delta\lambda$ n_{inc}”

a composite spectrum can be obtained. The function “ref_spec” acquires n_{inc} spectra starting at the wavelength λ in Å increasing by $\Delta\lambda$ in Å. The integration time to be used is determined by Δt (in units of 250 *ms*), the image format by f. By specifying appropriate parameters, spectra covering the full spectral range of the instrument on both the KBr and bare cathodes can be acquired. The Lyman-α line has, however, to be treated with care, i.e. it will be projected onto the attenuators on the detector and two images will be needed instead of one, in order to cover both wings.

A special case is the command

“celestial_obj t_{max} t_{stp} n_{img} $dark$ λ $\Delta\lambda$ n_{inc}”

It can be used to locate (search phase) and observe (study phase) celestial objects (stars, planets or comets) near the Sun. In preparation for “celestial_obj”, the 4×300-$arcsec^2$ slit has to be selected. The wavelength band to be used for detection has to be set up (by calling lambda11). The telescope has to be pointed to a position off the solar limb where the object can be expected to pass.

The “celestial_obj” initially determines the detection threshold value. If the parameter *dark* is negative, the threshold level is derived from a dark signal image acquired at the current position. A positive value gives the threshold value to be used.

In the search phase images are acquired by the instrument using an integration time of 40 % of the step time t_{stp} (in seconds). No data will be transmitted to the ground. If four consecutive images contain pixel values higher than twice the threshold value, the object has been detected and the study phase begins. If no object has been detected after the maximum search time t_{max} (in seconds) the function “celestial_obj” stops.

After the object has been located, the study phase begins. The centre of the slit will be pointed to the object location. To correct for the motion of the objects the telescope pointing will be changed in the E-W direction in steps of 0.76 *arcsec* every t_{stp} (for stars the value of t_{stp} will be about 18.5 *s*). For

1995SoPh..162..189W

planets and comets the user has to determine the step times, which can be positive or negative. In the latter case the stepping is in reversed direction.

In the study phase the object will be observed in n_{img} wavelength bands starting at λ (in $\AA$) and incrementing by $\Delta\lambda$ ($\AA$) in analogy to the "refspec" function. In every wavelength band n_{inc} images will be acquired with 1024 spectral and 12 spatial pixels and transmitted to the ground. The integration time is set to be 1.5 s less than t_{stp} to allow for the pointing to be updated between consecutive images. One image will be omitted whenever the wavelength is changed.

Finally, the flat-field mode should be mentioned. The flat-field correction can be determined onboard and can be applied before data compression schemes will be activated.

4.5. ONBOARD DATA STORAGE ASSESSMENTS

The short list of high-level commands discussed so far should, in principle, be sufficient to operate SUMER starting from its "standby mode". However, there are additional telemetry requirement considerations that might cause the user some difficulties. Obviously the user will have to define the scientifically relevant parameters for her/his study, such as spatial, spectral and temporal resolutions and line selection first. If the resolution requirements are not extreme and if only a small number of lines has to be observed, the standard telemetry rate of 10 $kbit\ s^{-1}$ science data will probably be adequate. With more demanding requirements in terms of resolution and number of lines, the rate will exceed the above threshold. Should a short observing sequence be envisaged, this need not worry the user as SUMER will be able to store up to 5 MB of data. This will be done by storing excess images for later transmission. In this fashion, the user receives in near-real time image data, albeit with reduced temporal resolution. Stored images will be dumped after completion of the sequence.

For observations with longer durations and high telemetry requirements, negotiations with CDS could lead to a telemetry mode change with a rate of 21 $kbit\ s^{-1}$ for SUMER. Alternatively, if this is not feasible or if co-operation with CDS is an essential part of the study, the spectral and/or spatial ranges to be covered must be reduced and data compression schemes have to be utilized. Note, however, that in this case the execution times presented in Section 4.1. have to be accommodated.

4.6. PREDEFINED OPERATIONAL PROGRAMMES (POP)

Predefined Operational Programmes are stored in the SUMER PROMs and transferred to the processor RAMs by the boot controller. The scientific definition of the POPs has been done over the years by a great number of investigators in response to requests issued in the SUMER Red Book. Table VI lists the POPs available in the SUMER flight software.

1995SoPh..162..189W

TABLE VI

Summary List of Predefined Operational Programmes (POP).

High-resolution line shifts
Line shift variation/line ratios
Line ratios at fixed location
Off-limb line profiles
Reference spectra
Full Sun imaging
Evolution of structures
Explosive events
Lyman-α ‘calibration’
Fine structure of a prominence
Ephemeral active regions
Bright point diagnostic
Active structure dynamics
Vector velocity fields off limb
Star spectra and coronal streamers
Turbulences and flows
Sunspot velocity fields
Magnetohydrodynamic waves
Forbidden/allowed line widths
Transition region and corona studies
Transition region and coronal emission relationship using Si III
N_e diagnostic using O IV, Si IV, Si V
N_e diagnostic using Ar VIII, Si VIII, and Fe XI off limb
Explosive events at different temperatures
Coronal mass ejection onset
Solar wind in a coronal hole
Sun grazing comet observation
Chromospheric network
Prominences and coronal mass ejections
Sub-second oscillations
Synoptic sequence
Transition region line intensities
Coronal magnetohydrodynamic turbulence
Temperature gradient in a coronal hole

It is beyond the scope of this contribution to describe all the POPs in detail and information should be sought in the SUMER Red Book and the SUMER Operations Guide. Here it will suffice to say that, in general, POP # M can be called, after the pointing has been set, by commanding

“init_POP_param M”
“start_POP M”.

POP # M will then run with its default parameters. Parameter changes can be implemented if needed.

4.7. USER DEFINED PROGRAMMES (UDP)

It can be expected that POPs, even if parameter changes are considered, will not be able to fulfill all observational requirements. It is, therefore, important to understand the concept of User Defined Programmes. UDPs have to be written in the SUMER Command Language and will, after verification, be uplinked to the instrument, where they will be executed in close analogy to the POPs. A simple example of such a programme is given in Appendix C to demonstrate the UDP concept. It was written in support of cross-calibration activities on SOHO and would acquire a total of 16 spectroheliogrammes at 584.33, 609.79, 770.41, 1215.67 and 1242.01 Å.

Up to 16 UDPs can reside in the instrument at a time and can be called by “Start-UDP X”. For further details the user should consult the SUMER Operations Guide.

5. Concluding Remarks

With SUMER, a high-resolution normal-incidence EUV spectrometer will be available on SOHO for studies of the solar atmosphere. The operation of the instrument is extremely flexible and, at the same time, sufficiently easy to manage. It is thus hoped that many scientific investigations can and will be performed with the help of this instrument and that SUMER will provide a significant contribution to the achievement of the science goals of SOHO.

Acknowledgements

The SUMER project is financially supported by BMFT/DARA, CNES, NASA and PRODEX (Swiss contribution). Additional financial support is being provided by the participating institutions along with general administrative assistance at various phases of the project. The instrument development has been carried out by a large dedicated team of engineers, scientists and technicians co-ordinated by a management support group. The SUMER investigators would like to thank J. Aboudarham, A. Arondel, S.J. Battel, C. Becker, L. Bemmann, H.-M. Bock, R. Boucarut, P. Boutry, P. Bouyries, H.-J. Braun, I. Büttner, I.E. Dammasch, A. Dannenberg, C. Diesch, W. Donakowski, D. Dumont, W. Engelhardt, H.-G. Engelmann, K. Eulig, A. Fischer, E. Frank, G.A. Gaines, D. Germerott, K. Gräbig, W. Grill, M.A. Gummin, J.W. Hamilton, H. Hartwig, E. Hertzberg, J. Hoberman, G. Hoch, J. Hollandt, J. Hull, P. Jelinsky, M. Jhabvala, H.G. Kellner, E. Keppler, R. Keski-Kuha, E. Korzac, D. Leviton, J. Linant, Y. Longval, O. v.d. Lühe, T. Magoncelli, C. Maurel, R. Meller, T. Moran, N. Morisset, N. Mosquet, N. Neisen, W. Neumann, J. Osantowski, A. Pauly, W. Paustian, J. Platzer, K. Poser, R. Raffanti, W. Reich, T. Rodriguez-Bell, T. Saha, T. Sasseen, H. Schild, R. Schmidt, H. Schüddekopf, H. Specht, E. Steinmetz, J.M. Stock, U. Strohmeyer, W. Tappert, W. Thompson, S. Töpfer, J.L. Tom, G. Tomasch, B. Wand, B. Welsh, and G. Wright for their contributions. The work of many contractors was essential in designing and manufacturing most of the sub-systems of SUMER and its flight and ground software. Particular mention should be made here of K. Lattner and E. Petit. Scientific advice was provided by a team of Associate Scientists: J. Aboudarham, B. Aschenbach, W.I. Axford, J. Barnstedt, F. Bely-Dubau, V. Bommier, J.L. Culhane, J.P. Delaboudiniere, C. Diesch, G. Doschek, J.G. Doyle, J. Dubau, B. Dwivedi, G. Einaudi, A. Fludra, B. Foing, P. Gouttebroze, R.A. Harrison, H.F. Haupt, E. Haug, J. Hollandt, W.-H. Ip, C. Jordan, O. Kjeldseth-Moe, B. Kliem, F.

Kneer, B. Leroy, I. Liede, O. v.d. Lühe, P. Maltby, H.E. Mason, R.W.P. McWhirter, P. Mein, F. Millier, B.E. Patchett, J.H. Parkinson, E.R. Priest, A.K. Richter, H. Rosenbauer, S. Sahal, D. Samain, B. Schmieder, J.H.M.M. Schmitt, M. Schüssler, R. Schwenn, G.M. Simnett, G. Tondello, J. Trümper, V.M. Vasyliunas, and O. Vilhu.

Appendix A. The SUMER Rear Slit Camera (RSC)

A schematic diagram of the optical arrangement of the rear slit camera is shown in Figure A-1. A 90°-deflection mirror is not shown.

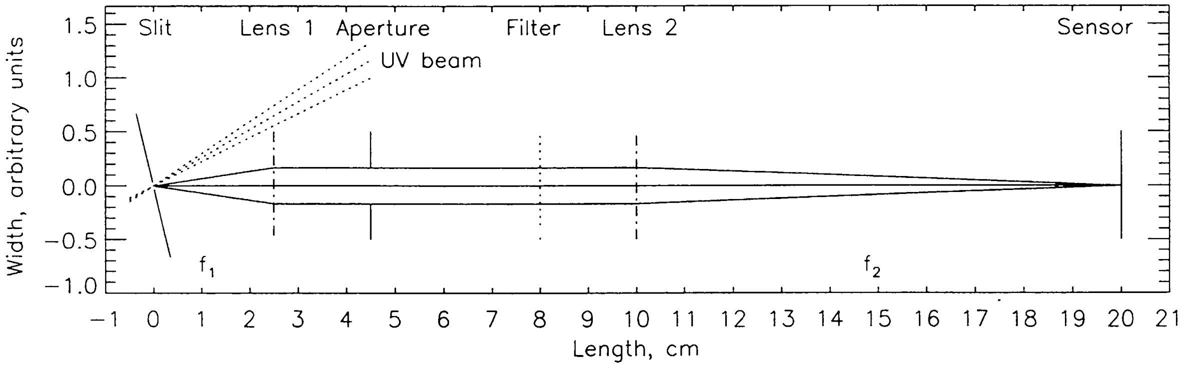

Fig. A-1. Schematic diagram of the Rear Slit Camera (RSC) optical system. The dimensions in width are not to scale. Nominal parameter values are: Angle of UV beam with respect to slit plane +2.5° to 6.5°, angle of RSC beam and slit plane −10°, focal length $f_1 = 25$ *mm*, focal length $f_2 = 100$ *mm*, aperture width 0.65 *mm*. Dimension in the out-of-plane direction are: Spectrometer slit length 1.89 *mm* (300 *arcsec*), aperture height 4.50 *mm* and 512 pixels of 25 μm each.

The focal length ratio of $f_2/f_1 = 4$ provides a magnification of the slit on the RSC sensor. The position of the solar limb can be determined to a fraction of an arcsecond both in perpendicular and in parallel configurations. The limb observations will give an accurate position of the centre of the Sun and can provide an important criterion for adjusting the slit focus position. Observations of sunspots could be relevant to the differential rotation correction, but will also be used to determine the solar rotation axis with respect to the SUMER internal co-ordinate system.

The spectral response of the RSC defined by its filter is given in Figure A-2 together with the solar spectral irradiance.

With a 1-*arcsec* slit, the RSC is adjusted to observe near the 2nd order maximum of the slit diffraction pattern. It should be noted that observations using the narrow slit of 0.3-*arcsec* width will also be possible. In this case, the observation will be near the 1st order maximum and, this being approximately a factor of three higher than that of the 2nd order, the intensity adjustment will not differ significantly from the nominal situation. Fine adjustment of the RSC intensity setting will be performed by selecting an appropriate integration time. Observations using the RSC can be performed independently of the operation of the UV spectrometer, but they can, if needed, also be done interspersed with UV observations. RSC data will be transmitted to the SUMER DPU with a rate of 156.25 *kbit* s^{-1} and will be sent to SOHO in the SUMER science telemetry channel.

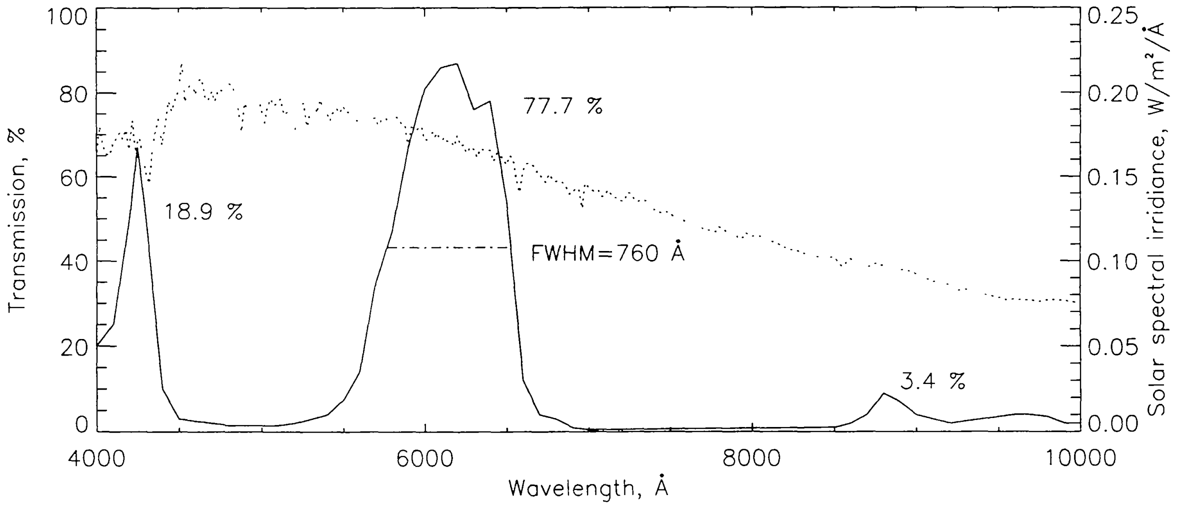

Fig. A-2. Transmission curve of the Rear Slit Camera (RSC) filter and the solar spectral irradiance. The relative contributions of the three transmission bands are also given.

Appendix B. Details on the Standard Rotation Compensation

The SUMER pointing co-ordinates x, y have to be transformed into a heliographic system (X', Y') before the necessary rotation compensation can be determined. With $R_\odot$, the solar radius (constant in this approximation), we obtain the seasonal variation of the sub-SOHO point with respect to the solar equator by a co-ordinate transformation with a tilt angle β (positive in the northern hemisphere), which will be updated from the ground on a weekly basis. Note that generally (X', Y') $\neq$ (X_{ii}, Y_{ii}) and that $x^2 + y^2 < R_\odot^2$ for observations on the solar disk.

The transformation yields

$$x' = x \quad \text{and}$$

$$y' = -y \; cos \; \beta + \sqrt{R_\odot^2 - (x^2 + y^2)} \; sin\beta$$

which then give

1995SoPh..162..189W

$$\theta = arcsin\ (y'/R_\odot)$$
$$\psi = arcsin\ (x'/(R_\odot cos\theta))$$

the heliographic latitude θ and longitude ψ (measured from the sub-SOHO meridian). These values will be used in the standard rotation compensation scheme. With

$$\omega(\theta) = g + h(sin^2\theta - sin^2 15^\circ)$$

where $g = 14.339^\circ$ day^{-1} and $h = -2.85^\circ$ day^{-1} (Balthasar et al., 1986) the differential rotation is taken into account. The synodic rotation frequency follows from

$$\omega_S(\theta) = \omega(\theta) - \omega_E$$

where $\omega_E = 0.98561^\circ$ day^{-1} is the mean sidereal orbital velocity of the Earth and ω_S is the synodic rotation frequency. Finally,

$$\hat{\omega}(\theta, \psi) = \omega_S(\theta)\ cos\psi$$

is the effective angular rotation frequency. A rotation compensation step of 0.76 *arcsec* will be performed in the $+x$ direction (towards the West) every

$$rc \approx \frac{0.76 * 86400}{3600} \frac{D}{\hat{\omega} R_\odot\ cos\theta} \quad [s]$$

where D is the mean distance between SOHO and the sub-SOHO point.

Appendix C. Example of a User Defined Programme (UDP)

```
/* SUMER in standby */
/* ================================= */
ExitOnError ALIAS if (Res < (INT32) 0) goto Exit; ifend
TIME1SEC ALIAS 4 /* integration time in units of 1/4 s */
P_STEP1 ALIAS 16 /* pointing steps in units of 1/16 arcsec */
INT_Time ALIAS 7.5 /* integration time 7.5 s */
/* wavelengths in Å to be observed * /
He_I ALIAS 584.33
Mg_X ALIAS 609.79
Ne_VIII ALIAS 770.409
H_I ALIAS 1215.67
Fe_XII ALIAS 1242.01
/* reference pixels */
He_px ALIAS 890
```

```
Mg_px ALIAS 910
Ne_px ALIAS 140
H_px ALIAS 1000
Fe_px ALIAS 430
main;
/* Declaration */
/* === Constant declarations ==================== */
/* === Definition and loading of programme parameters ======= */
REAL32 Ypos = (REAL32)ParamR(1);
/* Y position in arcmin (+ = W, - = E) */
REAL32 Zpos = (REAL32)ParamR(2);
/* Z position in arcmin (+ = N, - = S) */
/* === Variable declarations ========== * /
uINT8 rep;
INT16 Z, Y, Ref_Px[4] = {Mg_px, H_px, Mg_px, Fe_px};
INT32 Res;
REAL32 Line[4] = {Mg_X, H_I, Mg_X, Fe_XII};
Y = (INT16)(Ypos * 60 * P_STEP1); /* calculates Y pointing steps */
Z = (INT16)(Zpos * 60 * P_STEP1); /* calculates Z pointing steps */
/* Define SUMER configuration */
Res = slit (2); /* 1x300-arcsec^2 slit */
Res = point (Y,Z);
Res = rot_comp (-1.0) ; /* rotation compensation off */
Res = sphel_mode (0);/* no interruption */
Res = compression (5); /* quasilog – min-max */
Res = binning (1,1); /* no binning */
/* ———————————— */
for (rep = 0 to 3)
/* ———- Scan 1 and 2 ———- */
Res = lambda11 (He_px, He_I);
Res = lambda21 (Ref_Px[rep], Line[rep]);
Res = spectrohelio2 ((uINT16)(INT_Time * TIME1SEC), 12, 2, 79);
/* ———- Scan 3 and 4 ———- */
Res = lambda11 (Ne_px, Ne_VIII);
Res = lambda21 (Ne_px, Ne_VIII);
Res = spectrohelio2 ((uINT16)(INT_Time * TIME1SEC), 12, 2, 79);
forend;
Exit;
end;
```

References

Balthasar, H., Vázquez, M., and Wöhl, H.: 1986, *Astron. Astrophys.* **155**, 87.

Brückner, G.E., et al.: 1995, *this volume.*

Dammasch, I.E.: 1992, in *Data Analysis Workshop, Proc. of 4th ESO/ST-ECF No. 41*, 137.

Davila, J.M.: 1985, *Astrophys. J.* **291**, 328.

Delaboudinière, J.P., et al.: 1995, *this volume.*

Dwivedi, B.N.: 1994, *Space Sci. Rev.* **65**, 289.

Fraser, G.W., Pearson, J.F., and Lees, J.E.: 1987, *Nucl. Instrum. and Meth.* **A254**, 447.

Gabriel, A.H. and Jordan, C.: 1969, *Mon. Not. R. Astr. Soc.* **145**, 241.

Harrison, R.A., et al.: 1995, *this volume.*

Heroux, L. and Cohen, M.: 1971, *Phil. Trans. Roy. Soc. London* **A270**, 99.

Hollandt, J., Huber, M.C.E., and Kühne, M.: 1993, *Metrologia* **30**, 381.

Kohl, J.L., et al.: 1995, *this volume.*

Marsch, E.: 1994, *Adv. Space Res.* **14(4)**, 103.

Siegmund, O.H.W., Everman, E., Vallerga, J., Sokolowski, J., and Lampton, M.: 1987, *Applied Optics* **26(17)**, 3607.

Siegmund, O.H.W., Vallerga, J., and Wargelin, B.: 1988, *IEEE Trans. Nucl. Sci.* **NS-35**, 524.

Siegmund, O.H.W., and Gaines, G.: 1990, *Proc. SPIE* **1344**, 217.

Siegmund, O.H.W., Gummin, M.A., Stock, J., Marsh, D., Raffanti, R., Sasseen, T., Tom, J., Welsh, B., Gaines, G., Jelinsky, P., Hull, J., Higgens, B., Magoncelli, T., Hamilton, J.W., Battel, S.J., Poland, A.I., Jhabvala, M., Sizemore, K., and Shannon, J.: 1994, *Proc. SPIE* **2280**, 89.

Wentzel, D.G.: 1977, *Solar Phys.* **52**, 163.

Wilhelm, K., Curdt, W., Gabriel A.H., Grewing, M., Huber, M.C.E., Jordan, S.D., Kühne, M., Lemaire, P., Marsch, E., Poland, A.I., Schühle, U., Thomas, R.J., Timothy, J.G., and Vial, J.-C.: 1994, in *Solar Coronal Structures, Proc. of IAU Colloq. No. 144*, 619.